

# Exact decomposition of homoclinic orbit actions in chaotic systems: Information reduction

Jizhou Li<sup>1</sup> and Steven Tomsovic<sup>1</sup>

<sup>1</sup>*Department of Physics and Astronomy, Washington State University, Pullman, Washington 99164-2814, USA*  
(Dated: December 14, 2024)

Homoclinic and heteroclinic orbits provide a skeleton of the full dynamics of a chaotic dynamical system and are the foundation of semiclassical sums for quantum wave packet/coherent state and transport quantities. Here, the homoclinic orbits are organized according to the complexity of their phase space excursions, and exact relations are derived expressing the relative classical actions of complicated orbits as linear combinations of those with simpler excursions plus phase space cell areas bounded by stable and unstable manifolds. The total number of homoclinic orbits increases exponentially with excursion complexity, and the corresponding cell areas decrease exponentially in size as well. With the specification of a desired precision, the exponentially proliferating set of homoclinic orbit actions is expressible by a slower-than-exponentially increasing set of cell areas, which may present a means for developing greatly simplified semiclassical formulas.

## I. INTRODUCTION

Specific sets of rare classically chaotic orbits are central ingredients for sum rules in classical and quantum systems [1]. Classical sum rules over unstable periodic orbits describe various entropies, Lyapunov exponents, escape rates, and the uniformity principle [2]. Gutzwiller's trace formula [3] for quantum spectra is over unstable periodic orbits, closed orbit theory of atomic spectra [4, 5] gives the absorption spectrum close to the ionization threshold of atoms placed in magnetic fields, and heteroclinic (homoclinic) orbits arising from intersections between the stable and unstable manifolds of different (same) hyperbolic trajectories describe quantum transport between initial and final localized wave packets [6].

It is often the case that the nonlinear flows of phase space densities are completely captured by the stable and unstable manifolds of one or just a few short periodic orbits, hence also by the homoclinic and heteroclinic orbits that arise from intersections between these manifolds. These orbits can thus play the important role of providing a “skeleton” of transport for the system. It is not a unique choice, but each choice provides the same information. For example, an unstable periodic orbit gives rise to an infinity of homoclinic orbits, but it is also true that families of periodic orbits of arbitrary lengths accumulate on some point along every homoclinic orbit [7–9], and the periodic orbit points can be viewed as being topologically forced by the homoclinic point on which a particular sequence accumulates [10, 11].

Two problems are immediately apparent. The first is the particular importance of having accurate evaluations of classical actions because these quantities are divided by  $\hbar$  and play the role of phase factors for the interferences between terms, whose remainder after taking the modulus with  $2\pi$  must be  $\ll 2\pi$ . A straightforward calculation would proceed with the numerical construction of the actions, which would be plagued by the sensitive dependence on initial conditions for long orbits. An alternative method has been developed by the authors [11, 12].

That scheme converts the calculation of unstable periodic orbit actions into the evaluation of homoclinic orbit action differences. The homoclinic orbit actions can then be stably obtained as phase-space areas via the MacKay-Meiss-Percival principle [13, 14], or directly from the stable constructions of homoclinic orbits [9, 15–18]. In any case, this problem is essentially solved.

The second problem is more fundamental. Namely, the total number of periodic orbits increases exponentially with increasing period and for the homoclinic orbits with increasingly complicated excursions. This is a reflection of the non-vanishing rate of information entropy production associated with chaotic dynamics, which in an algorithmic complexity sense has been proven equivalent to the Kolmogorov-Sinai entropy [19–23], and hence the Lyapunov exponents via Pesin's theorem [24, 25]. On the other hand, entropies introduced for quantum systems [26–28] vanish due to the non-zero size of  $\hbar$ , if these systems are isolated, bounded, and not undergoing a measurement process. This gives one the intuitive notion and hope that there must be a means to escape the exponential proliferation problem of semiclassical sum rules.

Therefore, a scheme to replace classical and semiclassical sum rules that from the outset clearly have vanishing information entropy content is highly desirable [29]. The pseudo-orbits of the cycle expansion [1, 30, 31], the primitive orbits of Bogomolny's surface of section method [32], and multiplicative semiclassical propagator [33] were steps in this direction. Building on the methods of [11], we develop exact relations for the decomposition of homoclinic orbit relative actions with complicated excursions in terms of multiples of the two primary ones and sets of phase space areas. Accounting for an error tolerance determined by  $\hbar$  reduces the exponentially proliferating set of homoclinic orbit actions to combinations of an input set (i.e., phase space cell areas) that increase more slowly than exponentially (i.e., algebraically) with time.

This paper is organized as follows. Sec. II sets the background and introduces the basic concepts related to



the homoclinic tangle, horseshoe map, symbolic dynamics, and relative action functions. Sec. III reviews the concepts of winding number and transition time of homoclinic orbits, and introduces a hierarchical ordering of homoclinic points in terms of their winding numbers. Organizing the homoclinic points using the winding numbers, we identify an asymptotic scaling relation between families of homoclinic points, which puts strong constraints on the distribution of homoclinic points along the manifolds. Sec. IV gives two central results of this paper. The first one (Sec. IV B) is an exact formula for the complete expansion of homoclinic orbit actions in terms of primary homoclinic orbits and phase-space cell areas bounded by the manifolds. The second one (Sec. IV C) is the demonstration that a coarse-grained scale, determined by  $\hbar$ , allows for an approximation that eliminates exponentially small areas from the complete expansion, which gives an approximate action expansion that requires a subset of cell areas growing sub-exponentially.

## II. CONCEPTS AND DEFINITIONS

### A. Homoclinic tangle

For a simple visualization of the dynamics, consider a two-degree-of-freedom autonomous Hamiltonian system. With energy conservation and applying the standard Poincaré surface of section technique [34], the continuous flow leads to a discrete area-preserving map  $M$  on the two-dimensional phase space  $(q, p)$ . Assume the existence of a hyperbolic fixed point  $x = (q_x, p_x)$  under  $M$ :  $M(x) = x$ . Associated with it are the one-dimensional stable ( $S(x)$ ) and unstable ( $U(x)$ ) manifolds, which are the collections of phase-space points that approach  $x$  under successive forward and inverse iterations of  $M$ , respectively. Typically,  $S(x)$  and  $U(x)$  intersect infinitely many times and form a complicated pattern named *homoclinic tangle* [34–36], as partially illustrated in Fig. 1. Repeated use of this figure’s homoclinic point and region labels is made in the following.

Homoclinic tangles have been extensively studied as the organizing structures for classical transport and escape problems [13, 35–42]. Of particular interest are the homoclinic orbits, which lie along intersections between  $S(x)$  and  $U(x)$

$$h_0 = S(x) \cap U(x) \quad (1)$$

whose images under both  $M$  and  $M^{-1}$  approach  $x$  asymptotically:  $M^{\pm\infty}(h_0) = h_{\pm\infty} = x$ . The bi-infinite collection of images  $M^n(h_0) = h_n$ , is often referred to as a *homoclinic orbit*

$$\{h_0\} = \{h_{-\infty}, \dots, h_{-1}, h_0, h_1, \dots, h_{\infty}\}. \quad (2)$$

A *primary homoclinic point*,  $h_0$ , arises if the stable and unstable segments,  $S[h_0, x]$  and  $U[x, h_0]$ , intersect only

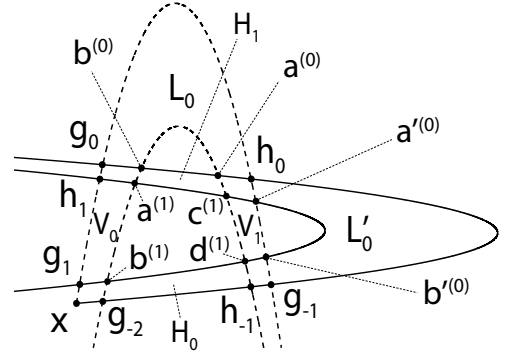


FIG. 1. Horseshoe-shaped homoclinic tangle formed by  $S(x)$  (dashed) and  $U(x)$  (solid), with two primary homoclinic orbits  $\{h_0\}$  and  $\{g_0\}$ . The vertical strips  $V_0$  and  $V_1$  are the generating partitions of the symbolic dynamics, and are mapped into the horizontal strips  $H_0$  and  $H_1$ , respectively, under one iteration. The fixed point  $x$  has symbolic string  $\bar{0}\bar{0}$ , and the primary homoclinic points  $h_0$  and  $g_0$  have symbolic strings  $01.1\bar{0}$  and  $01.0\bar{0}$ , respectively. Notice that the  $U(x)$  segments beyond  $g_0$  and  $h_1$  are simply connected and omitted from the figure for clarity, and the same for the  $S(x)$  segments beyond  $g_{-1}$  and  $h_{-1}$ .

at  $x$  and  $h_0$ . The resulting closed loop  $US[x, h_0] = U[x, h_0] + S[h_0, x]$  is topologically equivalent to a circle. As a result, the phase space excursions of the *primary homoclinic orbit*  $\{h_0\}$  takes the simplest possible form. It “circles” around the loop once from infinite past to infinite future. Figure 1 shows the simplest kind of homoclinic tangle having only two primary homoclinic orbits,  $\{h_0\}$  and  $\{g_0\}$ . In practice, more complicated homoclinic tangles are possible. However, generalizations are straightforward and not considered here.

The entire homoclinic tangle, as an infinite entity, can be constructed from iterations of finite segments on  $S(x)$  and  $U(x)$ . Identifying the *fundamental segments* as:

$$\begin{aligned} U_n &\equiv U[h_n, g_n] & U'_n &\equiv U(g_{n-1}, h_n) \\ S_n &\equiv S[h_n, g_{n-1}] & S'_n &\equiv S(g_n, h_n) \end{aligned} \quad (3)$$

$U_{n+k} = M^k(U_n)$  and similarly for  $U'_n$ ,  $S_n$ , and  $S'_n$ . The manifolds can be built as non-overlapping unions of the respective fundamental segments:

$$\begin{aligned} U(x) &= \bigcup_{n=-\infty}^{\infty} (U_n \cup U'_n) \\ S(x) &= \bigcup_{n=-\infty}^{\infty} (S_n \cup S'_n) \end{aligned} \quad (4)$$

and likewise for the homoclinic tangle. The topology of a homoclinic tangle contains important dynamical information, and is often studied over its truncations, namely a *trellis* [35, 36] defined as

$$T_{n_s, n_u} \equiv \left( \bigcup_{i=n_s}^{\infty} (S_i \cup S'_i) \right) \cup \left( \bigcup_{i=-\infty}^{n_u} (U_i \cup U'_i) \right) \quad (5)$$



where the integers  $n_s$  and  $n_u$  give the lower and upper bounds for the indices of the stable and unstable fundamental segments, respectively. For example, the pattern shown in Fig. 1 is  $T_{-1,1}$ , if the short segments,  $U(x)$  segment beyond  $g_1$ , and  $S(x)$  beyond  $g_{-2}$  are removed.

Given a trellis  $T_{n_s, n_u}$  and four homoclinic points  $a, b, c, d \in T_{n_s, n_u}$  that form a simple closed region bounded by the loop  $SUSU[a, b, c, d] = S[a, b] + U[b, c] + S[c, d] + U[d, a]$ , it is called a *cell* of  $T_{n_s, n_u}$  if there are no stable and unstable manifold segments from  $T_{n_s, n_u}$  that enter inside the region. Consequently, there are no homoclinic points other than the four vortices on the boundary of the cell. For example, both  $V_0$  and  $V_1$  are cells of  $T_{-1,0}$ . However, in  $T_{-1,1}$  they get partitioned by  $U_1$  and are not cells anymore since there are unstable segments inside them. Each trellis gives a specific partition to the phase space. By fixing the  $n_s$  value and increasing the  $n_u$  value, the resulting sequence of trellises yields a systematic and ever-finer partition of the phase space, which acts as the skeletal-like structures for the study of homoclinic orbits.

Of particular relevance to calculating the homoclinic orbit relative actions is the sequence of trellises  $T_{-1, n_u}$ , with  $n_u = 0, 1, \dots, N$ . New homoclinic points appear on  $S_{-1}$  upon each unit increase of  $n_u$ , and their relative actions are closely related to certain cell areas. In fact, of all the cell areas of  $T_{-1, n_u}$ , two subsets are relevant to the action calculations. The first subset, defined as *type-I* cells, are those from the region  $V_0$  partition. Equivalently, the type-I cells are those with two stable boundary segments located on  $S[x, g_0]$  and  $S[b^{(0)}, g_{-2}]$ , respectively. Similarly, the second subset, or the *type-II* cells, are those from the partition of the closed region bounded by  $SUSU[g_{-2}, b^{(0)}, a^{(0)}, h_{-1}]$ . Equivalently speaking, the type-II cells are those with two stable segments located on  $S[b^{(0)}, g_{-2}]$  and  $S[h_{-1}, a^{(0)}]$ , respectively. Figure 1 shows the examples of  $T_{-1,1}$ , a type-I cell bounded by  $SUSU[h_1, g_0, b^{(0)}, a^{(1)}]$  and a type-II cell bounded by  $SUSU[a^{(1)}, b^{(0)}, a^{(0)}, c^{(1)}]$ . Section IV B shows that the knowledge of these types of cell areas is sufficient for the action calculation of all homoclinic orbits.

For the study of chaotic transport, it is customary to define some special regions inside the homoclinic tangle, which govern the flux in and out of the tangle. Following the conventions [13, 36], the phase-space region bounded by loop  $US[x, g_0]$  is the *complex*, and the regions bounded by the loops  $US[h_n, g_n]$  and  $US[g_{n-1}, h_n]$  are *lobes* denoted by  $L_n$  and  $L'_n$ , respectively. The union of lobes  $L_0$  and  $L'_0$  is often called a *turnstile* [13].

A simplifying assumption adopted here is the “open system” condition [36, 38], which assumes the lobes  $L'_n$  and  $L_{-n}$  with  $n \geq 1$  extend out to infinity as  $n$  increases and never enter the complex region. Consequently, there are no homoclinic points distributed on the segments,  $S(g_n, h_n)$  and  $U(g_{n-1}, h_n)$ , which simplifies addressing the homoclinic orbits. However, this restriction is not essential and can be removed to accommodate closed systems as well.

## B. Symbolic dynamics

Symbolic dynamics [43–46] is a powerful construct that characterizes the topology of orbits in chaotic systems. In essence, it encodes the trajectories of various initial conditions under the mapping into infinite strings of alphabets, assigned using their phase space itineraries with respect to a generating Markov partition [47, 48]. Such a generating partition can be constructed from the homoclinic tangle. Assuming the system is highly chaotic and the homoclinic tangle forms a complete Smale’s horseshoe [49, 50], as the one depicted in Fig. 1. The generating partition is then the collection of two regions  $[V_0, V_1]$ , where  $V_0$  is the closed region bounded by  $USUS[x, g_{-2}, b^{(0)}, g_0] = U[x, g_{-2}] + S[g_{-2}, b^{(0)}] + U[b^{(0)}, g_0] + S[g_0, x]$ , and  $V_1$  is the closed region bounded by  $USUS[h_{-1}, g_{-1}, h_0, a^{(0)}]$ . The deformation of these regions under the dynamics can be visualized in a simple way: under one iteration of  $M$ , the curvy-rectangular region bounded by  $USUS[x, g_{-1}, h_0, g_0]$  is compressed along its stable boundary and stretched along its unstable boundary while preserving the total area, folded into an U-shaped region bounded by  $USUS[x, g_0, h_1, g_1]$  and overlap onto itself. During this process, the vertical strips  $V_0$  and  $V_1$  are mapped into the horizontal strips  $H_0$  and  $H_1$ , respectively, as labeled in Fig. 1. In the meantime, the middle region in between  $V_0$  and  $V_1$  bounded by  $USUS[g_{-2}, h_{-1}, a^{(0)}, b^{(0)}]$  is mapped into part of  $L'_0$  bounded by  $USUS[g_{-1}, h_0, a^{(0)}, b^{(0)}]$  and will escape the complex region under further iterations. The inverse mapping of  $M^{-1}$  has similar but reversed effects, with  $M^{-1}(H_i) = V_i$  ( $i = 0, 1$ ) and the region bounded by  $USUS[g_1, b^{(0)}, a^{(0)}, h_1]$  to escape.

Under the symbolic dynamics, each point  $z_0$  inside the complex that never escapes under forward and inverse mappings can be put into an one-to-one correspondence with a bi-infinite symbolic string

$$z_0 \Rightarrow \cdots s_{-2}s_{-1}.s_0s_1s_2 \cdots \quad (6)$$

where each digit  $s_n$  indicates the region that  $M^n(z_0)$  lies in:  $M^n(z_0) = z_n \in V_{s_n}$ , where  $s_n \in \{0, 1\}$ . The position of the decimal point indicates the present location of  $z_0$  since  $z_0 \in V_{s_0}$ . The symbolic string gives an “itinerary” of  $z_0$  under successive forward and inverse iterations, in terms of the regions  $V_0$  and  $V_1$  in which each iteration lies. The mapping  $M$  then corresponds to a Bernoulli shift on symbolic strings composed by “0”s and “1”s

$$M^n(z_0) \Rightarrow \cdots s_{n-2}s_{n-1}.s_n s_{n+1} s_{n+2} \cdots \quad (7)$$

therefore encoding the dynamics with simple strings of integers. Assume a complete horseshoe structure here in which all possible combinations of substrings exist, i.e. no “pruning” [51, 52] is needed.

The area-preserving Hénon map [53] is used as a confirmation of the theory and its approximations:

$$p_{n+1} = q_n, \quad q_{n+1} = a - q_n^2 - p_n. \quad (8)$$



With parameter  $a = 10$ , it gives rise to a complete horseshoe-shaped homoclinic tangle; see Fig. 1. As it satisfies both the complete horseshoe and open system assumptions, the theory is directly applicable. Nevertheless, the results derived ahead mostly carry over into more complicated systems possessing incomplete horseshoes [54], or systems with more than binary symbolic codes, though more work is needed to address such complications.

The fixed point  $x$  has the symbolic string  $x \Rightarrow \dots 0.0\dots = \bar{0}.\bar{0}$  where the overhead bar denotes infinite repetitions of “0”s since it stays in (on the boundary of)  $V_0$  forever. Consequently, other than the orbit containing the point  $\bar{0}1.\bar{0}$ , any homoclinic point  $h$  of  $x$  must have a symbolic string of the form

$$h \Rightarrow \bar{0}1s_{-m}\dots s_{-1}.s_0s_1\dots s_n1\bar{0} \quad (9)$$

along with all possible shifts of the decimal point. The  $\bar{0}$  on both ends means the orbit approaches the fixed point asymptotically. The orbit  $\{h\}$  can then be represented by the same symbolic string:

$$\{h\} \Rightarrow \bar{0}1s_{-m}\dots s_{-1}s_0s_1\dots s_n1\bar{0} \quad (10)$$

with the decimal point removed, as compared to Eq. (9). The finite symbolic segment “ $1s_{-m}\dots s_{-1}s_0s_1\dots s_n1$ ” is often referred to as the *core* of the symbolic code of  $h$ , with its length referred to as the *core length*. To be discussed in Appendix A, the core length is a measure of the length of the phase-space excursion of  $\{h\}$ .

The identification of symbolic strings associated with arbitrary homoclinic points, as well as the ordering of homoclinic points on the fundamental segments  $S_n$  or  $U_n$ , are non-trivial tasks in general. Pioneering works along this line can be found in [55], where the symbolic assignment and relative ordering of homoclinic points on  $S_0$  were explicitly given for the Hénon map. Refer to Fig. 3 of [55] for a nice pictorial demonstration. However, [55] starts from the anti-integrable limit [56, 57] and derives the results as continuations of the limit. In Appendix A, we introduce a different analytic scheme, which makes use of the hierarchical structure of the homoclinic tangle (see Sec. III) to provide the ordering of homoclinic points on  $S_{-1}$  in terms of their symbolic codes. Based on the symbolic codes of the two primary homoclinic points on  $S_{-1}$ , which are  $h_{-1} \Rightarrow \bar{0}.11\bar{0}$  and  $g_{-2} \Rightarrow \bar{0}.01\bar{0}$ , it recursively builds up the codes of the more complicated homoclinic orbits by adding certain symbolic strings of finite lengths to the primaries, according to their positions in the hierarchic structure. The results are equivalent to those of [55] upon changing the alphabets “0”  $\rightarrow$  “+” and “1”  $\rightarrow$  “−”. This approach naturally facilitates an important accumulation relation (introduced in Sec. IIIB) and thus better integrates into the scheme of the present work.

### C. Relative actions

The classical actions of homoclinic orbits are divergent as they come from the infinite sum over the generating functions associated with each iteration along the orbit. Hence, it is necessary to consider finite relative actions. For any phase space point  $z_n = (q_n, p_n)$  and its image  $M(z_n) = z_{n+1} = (q_{n+1}, p_{n+1})$ , the mapping  $M$  can be viewed as a canonical transformation that maps  $z_n$  to  $z_{n+1}$  while preserving the symplectic area, therefore a *generating (action) function*  $F(q_n, q_{n+1})$  can be associated with this transformation such that [13, 14]

$$\begin{aligned} p_n &= -\partial F / \partial q_n \\ p_{n+1} &= \partial F / \partial q_{n+1} . \end{aligned} \quad (11)$$

Despite the fact that  $F$  is a function of  $q_n$  and  $q_{n+1}$ , it is convenient to denote it as  $F(z_n, z_{n+1})$ . This should cause no confusion as long as it is kept in mind that it is the  $q$  variables of  $z_n$  and  $z_{n+1}$  that go into the expression of  $F$ . A special example is the generating function of the fixed point,  $F(x, x)$ , that maps  $x$  into itself under one iteration. For homoclinic orbits  $\{h_0\}$ , the *classical action* is the sum of generating functions between each step

$$\mathcal{F}_{\{h_0\}} \equiv \lim_{N \rightarrow \infty} \sum_{n=-N}^{N-1} F(h_n, h_{n+1}) \quad (12)$$

However, according to the MacKay-Meiss-Percival action principle [13, 14], convergent relative actions can be obtained by comparing the classical actions of a homoclinic orbit pair:

$$\begin{aligned} \Delta \mathcal{F}_{\{h'_0\}\{h_0\}} &\equiv \lim_{N \rightarrow \infty} \sum_{n=-N}^{N-1} [F(h'_n, h'_{n+1}) - F(h_n, h_{n+1})] \\ &= \int_{U[h_0, h'_0]} p dq + \int_{S[h'_0, h_0]} p dq = \mathcal{A}_{US[h_0, h'_0]}^\circ \end{aligned} \quad (13)$$

where the  $\circ$  superscript in the last term indicates that the area evaluated is interior to a path that forms a closed loop, and the subscript indicates the path:  $US[h_0, h'_0] = U[h_0, h'_0] + S[h'_0, h_0]$ . Such an action difference is referred to as the *relative action* between  $\{h'_0\}$  and  $\{h_0\}$ . A special case of interest is the relative action between a homoclinic orbit  $\{h_0\}$  and the fixed point itself  $\{x\}$ :

$$\begin{aligned} \Delta \mathcal{F}_{\{h_0\}\{x\}} &= \lim_{N \rightarrow \infty} \sum_{n=-N}^{N-1} [F(h_n, h_{n+1}) - F(x, x)] \\ &= \mathcal{A}_{US[x, h_0]}^\circ \end{aligned} \quad (14)$$

which gives the action of  $\{h_0\}$  relative to the fixed point orbit action, and is simply referred to as the relative action of  $\{h_0\}$ .



A generalization of Eq. (14) applies to four arbitrary homoclinic orbits of  $x$ , namely  $\{a_0\}$ ,  $\{b_0\}$ ,  $\{c_0\}$ , and  $\{d_0\}$ . Expressing the relative actions of each of them using Eq. (14), and calculating the action difference between the following two pairs of orbits gives

$$\begin{aligned} & (\Delta\mathcal{F}_{\{a_0\}\{x\}} - \Delta\mathcal{F}_{\{b_0\}\{x\}}) - (\Delta\mathcal{F}_{\{c_0\}\{x\}} - \Delta\mathcal{F}_{\{d_0\}\{x\}}) \\ &= (\mathcal{A}_{US[x,a_0]}^\circ - \mathcal{A}_{US[x,b_0]}^\circ) - (\mathcal{A}_{US[x,c_0]}^\circ - \mathcal{A}_{US[x,d_0]}^\circ) \\ &= \mathcal{A}_{SUSU[a_0,c_0,d_0,b_0]}^\circ \end{aligned} \quad (15)$$

where

$$\begin{aligned} \mathcal{A}_{SUSU[a_0,c_0,d_0,b_0]}^\circ &\equiv \int_{S[a_0,c_0]} pdq + \int_{U[c_0,d_0]} pdq \\ &+ \int_{S[d_0,b_0]} pdq + \int_{U[b_0,a_0]} pdq \end{aligned} \quad (16)$$

is the curvy parallelogram area bounded by alternating segments of  $S(x)$  and  $U(x)$  connecting the four homoclinic points.

### III. HIERARCHICAL STRUCTURE OF HOMOCLINIC POINTS

#### A. Winding numbers and transit times

The infinite set of homoclinic orbits can be put into a hierarchical structure, organized using a winding number [58, 59] that characterizes the complexity of phase-space excursion of each individual orbit. The winding number of a homoclinic point  $h$  is defined to be the number of single loops (i.e., loops with no self-intersection) that the loop  $US[x, h]$  can be decomposed into [59]. The primary homoclinic points  $h_0$  and  $g_0$  points in Fig. 1 are associated with orbits having winding number 1, since both  $US[x, h_0]$  and  $US[x, g_0]$  are single loops. They form the complete first hierarchical family.

The non-primary homoclinic points  $a^{(0)}$  and  $b^{(0)}$  are both associated with winding number 2; i.e. the loop  $US[x, a^{(0)}] = US[x, h_0] + US[h_0, a^{(0)}]$ , both of which are single loops; and similarly for  $b^{(0)}$ ,  $US[x, b^{(0)}] = US[x, g_0] + US[g_0, b^{(0)}]$ . All points on a particular orbit are associated with the same winding number. Roughly speaking, a winding- $n$  orbit “circles” inside the complex region  $n$  times from the infinite past to the infinite future, and therefore the winding number characterizes the complexity of its phase-space excursion. Figure 1 of Ref. [59] has a nice illustration.

Within each family, the orbits can be further organized by their *transit times* [35, 36], which contains the length of the phase-space excursion of a homoclinic orbit. With the “open system” assumption, there are no homoclinic points on segments  $U'_n$  and  $S'_n$ . Therefore, any homoclinic point  $z_0$  must arise from the intersection between

some  $U_n$  and  $S_m$  segments, with  $n$  and  $m$  being appropriate integers such that  $z_0 \in U_n \cap S_m$ . The transit time of  $\{z_0\}$ , denoted by  $t$ , is defined as the difference in the indices of  $U_n$  and  $S_m$ :  $t = (n - m)$ . It can be interpreted as the length of the phase space excursion of the orbit. Starting from  $z_{-n} \in U_0 \cap S_{m-n}$ , and mapping  $t$  times,  $M^t(z_{-n}) = z_{-m} \in U_{n-m} \cap S_0$ . Thus,  $t$  is the number of iterations needed to map the orbit from  $U_0$  to  $S_0$ , which reflects the length of its excursion. Note that, excluding the primary homoclinic orbits,  $\{g_0\}$  and  $\{h_0\}$ , all homoclinic orbits have positive definite  $t$  since there are no intersections of  $U_n$  with  $S_0$  with negative integer  $n$  or 0; i.e. the first intersection of  $S_0$  is with  $U_1$ .

Since the mapping preserves the topology:  $M^k(z_0) = z_k \in U_{n+k} \cap S_{m+k}$ , every orbit  $\{z_0\}$  has one and only one point (which is  $z_0$ ) on  $S_m$ . Therefore, enumerating homoclinic points on  $S_m$  is equivalent to enumerating all distinct homoclinic orbits in the trellis. In practice, due to the natural shape of the homoclinic tangle, it is convenient to choose  $m = -1$ . Equivalently, all homoclinic points on  $S_{-1}$  with a maximum  $t = n+1$  are intersections with the trellis  $T_{-1,n}$  ( $= T_{-1,t-1}$ ). The total number of homoclinic orbits increases exponentially rapidly with the transit time. For example, in Fig. 2,  $U_0$  intersects  $S_{-1}$  at two points:  $a^{(0)}$  and  $b^{(0)}$ .  $U_1$  intersects  $S_{-1}$  at four points  $a^{(1)}$ ,  $b^{(1)}$ ,  $c^{(1)}$  and  $d^{(1)}$ . Furthermore,  $U_2$  intersects  $S_{-1}$  at eight points, where the four points  $a^{(2)}$ ,  $b^{(2)}$ ,  $c^{(2)}$  and  $d^{(2)}$  are winding-2, and the remaining four points, on the upper half of  $S_{-1}$  are not explicitly labeled and are winding-3. Including  $g_{-2}$  and  $h_{-1}$ , the total number of homoclinic points on  $S_{-1}$  is exactly  $e^{(t+1) \ln 2}$ .

#### B. Asymptotic accumulation of homoclinic points

Although homoclinic tangles create unimaginably complicated phase-space patterns, their behaviors are highly constrained by a few simple rules of Hamiltonian chaos, namely exponential compression and stretching occurs while preserving phase-space areas, and manifolds cannot intersect themselves or other manifolds of the same type. Therefore, locally near any homoclinic point, unstable (stable) manifolds form fine layers of near-parallel curves, with distances in between the curves scaling down exponentially rapidly as they get closer towards that point. As numerically demonstrated by Eq. (10) in [59], such asymptotic scaling relations exist inside every family of homoclinic points. A concrete mathematical description of this phenomenon is given by Lemma 2 in Appendix. B. 3 of [38], which states “iterates of a curve intersecting the stable manifold approach the unstable manifold.” Refer to Appendix. B for a brief overview of the lemma.

The asymptotic scaling ratio of the accumulation is determined by the stability exponent of the hyperbolic fixed point,  $\mu_x$ , as in Eq. (B1). Starting from Eq. (B1), let the  $z_u$  base point be  $g_{-2}$  in Fig. 2, and the curve  $\bar{C}$  that passes through  $z_u$  be the stable manifold segment



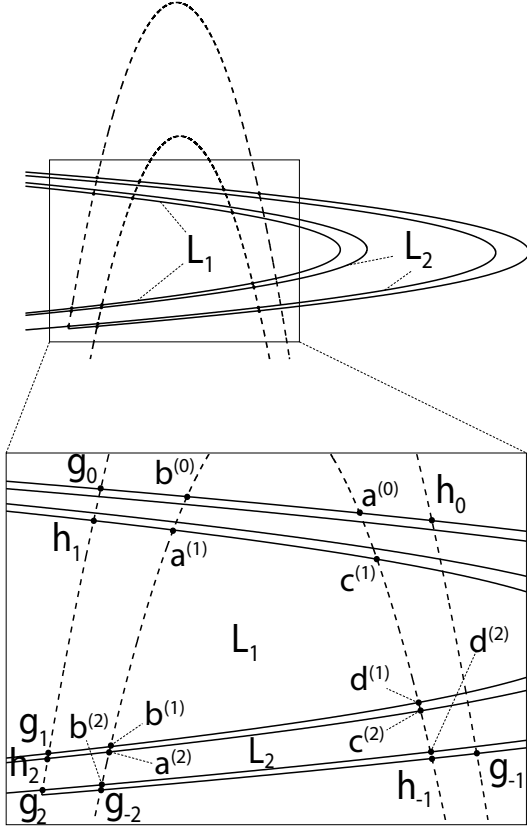


FIG. 2. Upper panel: trellis  $T_{-1,2}$ . Lower panel: (Zoomed-in) The hierarchy of homoclinic points on  $S_{-1}$  can be organized as the following: the winding-1 points  $g_{-2}$  and  $h_{-1}$  constitute the first-order family. The sequence of winding-2 points  $a^{(n)}$  and  $b^{(n)}$  ( $n \geq 0$ ) form two second-order families that accumulate on  $g_{-2}$  asymptotically under Eqs. (17) and (18). Similarly on the right side of  $S_{-1}$ , we have the winding-2 points  $c^{(n)}$  and  $d^{(n)}$  ( $n \geq 1$ ) accumulating on  $h_{-1}$ , which form two second-order families as well. Consequently, three families of areas  $[\mathcal{A}_{SU[SU[g_{-2}, b^{(n)}, d^{(n)}, h_{-1}]}^\circ]$ ,  $[\mathcal{A}_{SU[SU[b^{(n)}, a^{(n)}, c^{(n)}, d^{(n)}]}^\circ]$  and  $[\mathcal{A}_{SU[SU[a^{(n)}, b^{(n-1)}, d^{(n-1)}, c^{(n)}]}^\circ]$  accumulate on the bottom segment  $U[g_{-2}, h_{-1}]$  under Eq. (21), with the same asymptotic exponent  $\mu_x$ .  $L_1$  and  $L_2$  are the propagated lobes of the turnstile defined in the text at the end of Sect. IIA.

from  $S_{-1}$  that passes through  $g_{-2}$ . Furthermore, choose the  $C_0$  curve to be  $U_0$ , which intersects  $S_{-1}$  at  $a^{(0)}$  and  $b^{(0)}$ . The pair of points  $a^{(0)}$  and  $b^{(0)}$  here play the role of the  $z^{(0)}$  point in Fig. 14, which are the leading terms of the two families of winding-2 homoclinic points  $[a^{(n)}]$  and  $[b^{(n)}]$ , respectively, that accumulate asymptotically on  $g_{-2}$ . The two families of points  $[a^{(n)}]$  and  $[b^{(n)}]$  are generated from iterating  $U_0$  forward and intersecting the successive images  $U_n$  ( $n \in \mathbb{Z}^+$ ) with  $S_{-1}$ , and are located on the upper and lower side of  $U_n$ , respectively. The accumulation can be expressed in the asymptotic relation:

$$\begin{aligned} \lim_{n \rightarrow \infty} a^{(n)} &= g_{-2} \\ \lim_{n \rightarrow \infty} |a^{(n)} - g_{-2}| e^{n\mu_x} &= C(g_{-2}, a^{(0)}) \end{aligned} \quad (17)$$

where  $\|\cdot\|$  is the standard Euclidean vector norm, and  $C(g_{-2}, a^{(0)})$  is a positive constant depending on the base point  $g_{-2}$  and the leading term  $a^{(0)}$  in the asymptotic family. Similarly for  $b^{(n)}$  we have

$$\begin{aligned} \lim_{n \rightarrow \infty} b^{(n)} &= g_{-2} \\ \lim_{n \rightarrow \infty} |b^{(n)} - g_{-2}| e^{n\mu_x} &= C(g_{-2}, b^{(0)}) \end{aligned} \quad (18)$$

Notice that Eqs. (17) and (18) are obtained directly from Eq. (B1), by the substitutions  $z_u \rightarrow g_{-2}$  and  $z^{(n)} \rightarrow a^{(n)}/b^{(n)}$ . Therefore, the two families of winding-2 homoclinic points  $[a^{(n)}]$  and  $[b^{(n)}]$  accumulate asymptotically onto the winding-1 point  $g_{-2}$  along the stable manifold, under the scaling relations described by Eqs. (17) and (18). These relations will be denoted symbolically as

$$\begin{aligned} a^{(n)} &\xrightarrow[S]{n+1} g_{-2} \\ b^{(n)} &\xrightarrow[S]{n+1} g_{-2} \end{aligned} \quad (19)$$

where the  $\xrightarrow[S]{n+1}$  symbol indicates  $a^{(n)}$  and  $b^{(n)}$  are the  $(n+1)$ th member of their respective families,  $[a^{(0)}, a^{(1)}, \dots]$  and  $[b^{(0)}, b^{(1)}, \dots]$ , that accumulate on  $g_{-2}$  along the stable manifold with asymptotic exponent  $\mu_x$ .

Due to the same reasons, on the right side of  $S_{-1}$ , there are two families of winding-2 homoclinic points  $[c^{(n)}]$  and  $[d^{(n)}]$  ( $n \geq 1$ ) that accumulate asymptotically along the stable manifold on the winding-1 point  $h_{-1}$  under scaling relations similar to Eqs. (17) and (18):

$$\begin{aligned} c^{(n)} &\xrightarrow[S]{n} h_{-1} \\ d^{(n)} &\xrightarrow[S]{n} h_{-1} . \end{aligned} \quad (20)$$

An important consequence of the above asymptotic relations between homoclinic points is that the phase space areas spanned by them also scale down at the same rate. Using the present example, three families of areas can be easily identified, which are  $[\mathcal{A}_{SU[SU[g_{-2}, b^{(n)}, d^{(n)}, h_{-1}]}^\circ]$ ,  $[\mathcal{A}_{SU[SU[b^{(n)}, a^{(n)}, c^{(n)}, d^{(n)}]}^\circ]$ , and  $[\mathcal{A}_{SU[SU[a^{(n)}, b^{(n-1)}, d^{(n-1)}, c^{(n)}]}^\circ]$  ( $n \geq 2$ ). Each follows the scaling relation,

$$\lim_{n \rightarrow \infty} \frac{\mathcal{A}_{SU[SU[g_{-2}, b^{(n)}, d^{(n)}, h_{-1}]}^\circ}{\mathcal{A}_{SU[SU[g_{-2}, b^{(n+1)}, d^{(n+1)}, h_{-1}]}^\circ} = e^{\mu_x}. \quad (21)$$

with the same  $\mu_x$ . These areas are all from the partition of the lobe  $L'_{-1}$  using successively propagated lobes  $L_n$ . Returning to Fig. 2, where successive intersections between the fundamental segments  $U_n$  and  $S_{-1}$  of Eq. (3) accumulate on  $g_{-2}$  and  $h_{-1}$ , the following three identifications can be made:  $\mathcal{A}_{SU[SU[g_{-2}, b^{(n)}, d^{(n)}, h_{-1}]}^\circ$  is the area between the lower side of  $U_n$  and  $U[g_{-2}, h_{-1}]$ ,  $\mathcal{A}_{SU[SU[b^{(n)}, a^{(n)}, c^{(n)}, d^{(n)}]}^\circ$  is the area between the lower and upper sides of  $U_n$ , and  $\mathcal{A}_{SU[SU[a^{(n)}, b^{(n-1)}, d^{(n-1)}, c^{(n)}]}^\circ$  is the



area between the upper side of  $U_n$  and the lower side of  $U_{n-1}$ . As more lobes are added, such areas approach  $U[g_{-2}, h_{-1}]$ , and ratio  $e^{\mu_x}$  becomes almost exact. Hence Eq. (21) can be understood as an asymptotic relation between area partitions of  $L'_{-1}$  in the neighborhood of  $U[g_{-2}, h_{-1}]$ .

The above relations are obtained by choosing the  $z_u$  base point in Eq. (B1) to be the winding-1 points  $g_{-2}$  and  $h_{-1}$ , and studying the accumulations of winding-2 homoclinic points on them. Generally speaking, since the choice of the  $z_u$  base point is arbitrary, one can just as well choose  $z_u$  to be a winding- $m$  homoclinic point on  $U(x)$ , and there will always be two families of winding- $(m+1)$  homoclinic points that accumulate on  $z_u$  along  $S(x)$  under similar relations, with the same scaling ratio  $e^{\mu_x}$ . Therefore, Eq.(21) holds for any winding- $m$  homoclinic point and the winding- $(m+1)$  families of areas that accumulate on it. Take the example of Fig. 3, where the lobe  $L_3$  is added into the homoclinic tangle, which further partitions  $L'_{-1}$  and creates more homoclinic points on  $S_{-1}$ . Choosing the winding-2 point  $a^{(0)}$  as the base point, we can identify two families of winding-3 points,  $[e^{(n)}]$  and  $[f^{(n)}]$  ( $n \geq 1$ ) that come from  $U_{n+1} \cap S_{-1}$ , which accumulate on  $a^{(0)}$  with asymptotic ratio  $e^{\mu_x}$ . The same is true for the winding-3 families  $[r^{(n)}]$ ,  $[s^{(n)}]$  that accumulate on  $b^{(0)}$ . Consequently, in completely analogy to Eq. (21), three families of areas  $[\mathcal{A}_{SUSU[a^{(0)}, e^{(n)}, r^{(n)}, b^{(0)}]}^\circ]$ ,  $[\mathcal{A}_{SUSU[e^{(n)}, f^{(n)}, s^{(n)}, r^{(n)}]}^\circ]$ , and  $[\mathcal{A}_{SUSU[f^{(n)}, e^{(n-1)}, r^{(n-1)}, s^{(n)}]}^\circ]$  ( $n \geq 2$ ) accumulate on  $U[a^{(0)}, b^{(0)}]$  and each scales identically as,

$$\lim_{n \rightarrow \infty} \frac{\mathcal{A}_{SUSU[a^{(0)}, e^{(n)}, r^{(n)}, b^{(0)}]}^\circ}{\mathcal{A}_{SUSU[a^{(0)}, e^{(n+1)}, r^{(n+1)}, b^{(0)}]}^\circ} = e^{\mu_x}, \quad (22)$$

which gives the asymptotic area relations in the neighborhood of  $a^{(0)}$  and  $b^{(0)}$ . Such relations are true in the neighborhood of any homoclinic point, and they imply that the computation of a few leading area terms in any  $[\mathcal{A}_{SUSU[\dots]}^\circ]$  family suffices to determine the rest of the areas, depending on the desired degree of accuracy.

An important subtlety in the scaling relations concerns the exponent  $\mu_x$ . Due to the exponential compressing and stretching nature of chaotic dynamics, it is well-known that the new cell areas bounded by adjacent stable and unstable segments from a trellis with increasing iteration numbers must become exponentially small. See Appendix A of Ref. [12] for a brief review. In particular, one can anticipate that the new cell areas from  $T_{-1,n}$  decrease on average similarly to the horizontal strips  $H_{s_{-n} \dots s_{-1}}$  in Figs. 3 and 4 of Ref. [12], which scale at the rate  $e^{-n\mu}$ , where  $\mu$  is the system's Lyapunov exponent. However, in general  $\mu_x \neq \mu$ ,  $\mu_x$  measuring the stretching rate of the hyperbolic fixed point, which is expected to be  $\geq \mu$ . This begs the question as to how this could be consistent. In Sec. IIID, it is shown that this presumably larger exponent  $\mu_x$  only applies to calculating the ratios between successive areas within the specific families such as those in Eqs (21) and (22). Between dif-

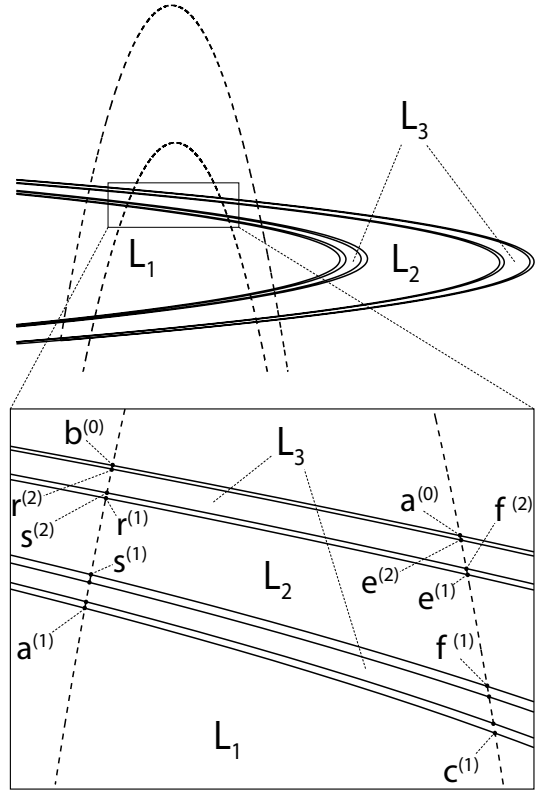


FIG. 3. Homoclinic tangle with  $U_1$ ,  $U_2$  and  $U_3$  present.  $L_3$  is stretched into a thin, long shape that extends along  $U(x)$  that wraps around  $U_1$ . The lower panel is the zoom of the box region from the upper panel, where the winding-3 points  $e^{(n)}$ ,  $f^{(n)}$ ,  $r^{(n)}$  and  $s^{(n)}$  come from  $U_{n+1} \cap S_{-1}$  ( $n = 1, 2$ ). The two families  $[e^{(n)}]$  and  $[f^{(n)}]$  accumulate on the winding-2 point  $a^{(0)}$ , and the families  $[r^{(n)}]$  and  $[s^{(n)}]$  accumulate on the winding-2 point  $b^{(0)}$  under the ratio  $e^{\mu_x}$ . Consequently, similar to the case in Fig. 2, there are three area families that accumulate on segment  $U[a^{(0)}, b^{(0)}]$  under Eq. (22),  $[\mathcal{A}_{SUSU[a^{(0)}, e^{(n)}, r^{(n)}, b^{(0)}]}^\circ]$ ,  $[\mathcal{A}_{SUSU[e^{(n)}, f^{(n)}, s^{(n)}, r^{(n)}]}^\circ]$ , and  $[\mathcal{A}_{SUSU[f^{(n)}, e^{(n-1)}, r^{(n-1)}, s^{(n)}]}^\circ]$ .

ferent families, the scaling exponents change to smaller values, which is consistent with the Lyapunov exponent being smaller than  $\mu_x$ . A shorthand reference to this is to say that Eqs. (21) and (22) are fast scaling relations, in the sense that they happen at faster rates than the average instability of the system as a whole,  $\mu$ .

Identical scaling results hold under the inverse mapping  $M^{-1}$  upon switching the roles of the stable and unstable manifolds. Shown in Fig. 4 is a simple example of the inverse case, where families of homoclinic points accumulate along the unstable manifold. For convenience, the  $a^{(0)}$  and  $b^{(0)}$  points from Fig. 2 are relabeled in this figure as  $v^{(-1)}$  and  $w^{(-1)}$ , respectively. Successive inverse mappings of  $S_{-1}$  intersect with  $U_0$  and create two families of winding-2 points  $[v^{(-n)}]$  and  $[w^{(-n)}]$  ( $n \geq 1$ ), which accumulate on the primary point  $g_0$  along the unstable manifold, under scaling relations similar to Eq. (17). Similar



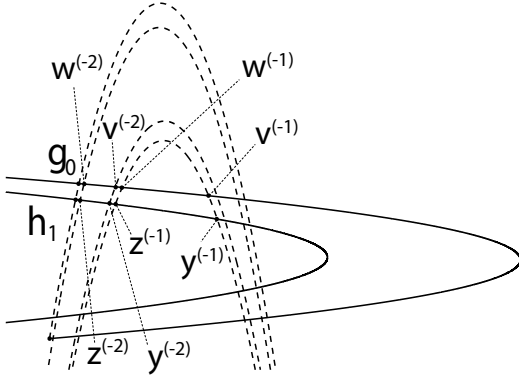


FIG. 4. Accumulation of homoclinic points along  $U(x)$  under  $M^{-1}$ . Two families of homoclinic points  $[v^{(-n)}]$  and  $[w^{(-n)}]$  are created from  $S_{-n} \cap U_0$ , that accumulate on  $g_0$  along  $U_0$ . Notice that only the  $n = 1, 2$  cases are plotted here. Similarly, the two families  $[y^{(-n)}]$  and  $[z^{(-n)}]$  are created from  $S_{-n} \cap U_1$ , and accumulate on  $h_1$  along  $U_1$ .

to Eq. (19), the accumulation along  $U(x)$  is denoted by

$$\begin{aligned} v^{(-n)} &\xrightarrow[n]{U} g_0 \\ w^{(-n)} &\xrightarrow[n]{U} g_0 \end{aligned} \quad (23)$$

where  $\xrightarrow[n]{U}$  indicates that  $v^{(-n)}$  and  $w^{(-n)}$  are the  $n$ th member of their respective families,  $[v^{(-1)}, v^{(-2)}, \dots]$  and  $[w^{(-1)}, w^{(-2)}, \dots]$ , that accumulate on  $g_0$  along the unstable manifold with asymptotic exponent  $\mu_x$ .

Also shown in Fig. 4 are other two families of winding-2 points  $[y^{(-n)}]$  and  $[z^{(-n)}]$  generated from  $S_{-n} \cap U_1$ , which accumulate on  $h_1$  along the unstable manifold. Notice that points  $y^{(-1)}$  and  $z^{(-1)}$  are identical to  $c^{(1)}$  and  $a^{(1)}$  from Fig. 2, respectively. Consequently, three families of areas  $[\mathcal{A}_{SUSU[h_1, g_0, w^{(-n)}, z^{(-n)}]}^\circ]$ ,  $[\mathcal{A}_{SUSU[z^{(-n)}, w^{(-n)}, v^{(-n)}, y^{(-n)}]}^\circ]$ , and  $[\mathcal{A}_{SUSU[y^{(-n)}, v^{(-n)}, w^{(-n+1)}, z^{(-n+1)}]}^\circ]$  ( $n \geq 2$ ) accumulate on  $S[h_1, g_0]$  under the asymptotic ratio  $e^{\mu_x}$ , similar to Eqs. (21) and (22). Therefore, the asymptotic behaviors of the manifolds between  $M$  and  $M^{-1}$  are identical, upon interchanging the roles of  $S(x)$  and  $U(x)$ . We would like to emphasize that this is a general result that comes from the stability analysis of the system, which holds true whether the system is time-reversal symmetric or not.

There is an interesting special case of the accumulation relations for which  $z_u$  is chosen to be the fixed point  $x$  itself. For this case, the primary orbits  $\{g_i\}$  and  $\{h_i\}$  themselves become two families of homoclinic points that accumulate on  $x$  with asymptotic ratio  $e^{\mu_x}$  under both forward and inverse mappings:

$$\begin{aligned} h_i &\xrightarrow[S]{} x, \\ g_i &\xrightarrow[S]{} x, \end{aligned} \quad (24)$$

and

$$\begin{aligned} h_{-i} &\xrightarrow[U]{} x, \\ g_{-i} &\xrightarrow[U]{} x \end{aligned} \quad (25)$$

although the meaning of the order number for each point inside these two families now becomes ambiguous, therefore removed from the top of the “ $\xrightarrow{\phantom{x}}$ ” sign. The hyperbolic fixed point  $x$  is now viewed as a “homoclinic point” of winding number 0, on which the winding-1 primaries accumulate.

### C. Partitioning of cell areas

In the partitioning of cell areas from increasing trelises, there are families of areas corresponding to fast and slow scaling relations. Since the homoclinic orbit actions are ultimately expressed using these areas, an investigation of this kind is crucial for the understanding of asymptotic clustering of homoclinic orbit actions. The partitioning process is recursive in nature, and the partition of the existing cells of  $T_{-1,n}$  by  $T_{-1,n+1}$  is the critical step. This process eventually leads to an organization of the cells into tree-like structures, and a classification of the scaling rates using the branches of the trees. These structures are identical for the type-I and type-II cells introduced in the discussion of Fig. 1, so it suffices to concentrate mostly on the type-I cells.

The partition starts from  $T_{-1,0}$ , where the only type-I cell is  $V_0$ . In order to introduce a partition subscript,  $V_0$  is denoted  $A$ . In the next iteration,  $A$  is partitioned by  $T_{-1,1}$ , in which the lobe  $L_1$  enters  $A$  dividing it into three finer cells, namely  $A_\alpha$ ,  $A_\beta$ , and  $A_\gamma$ , as shown in Fig. 5. Similarly, denote the cell area of  $T_{-1,0}$  enclosed by  $SUSU[g_{-2}, b^{(0)}, a^{(0)}, h_{-1}]$  by  $B$ .  $B$  is partitioned by

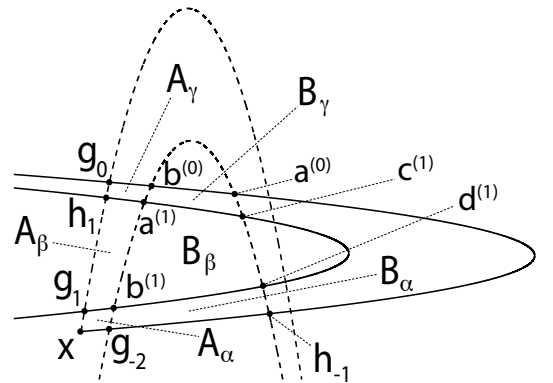


FIG. 5. The  $A$  cell from  $T_{-1,0}$  is partitioned into three cell areas in  $T_{-1,1}$ :  $A = A_\alpha + A_\beta + A_\gamma$ . Similarly for the type-II cell,  $B = B_\alpha + B_\beta + B_\gamma$ .

$T_{-1,1}$  in an identical way:  $B = B_\alpha + B_\beta + B_\gamma$  since the unstable lobes always enter the type-I and type-II regions simultaneously for the complete horseshoe map, and also for a large class of incomplete horseshoe maps as well.



In the next iteration,  $T_{-1,2}$  introduces finer partitions in which  $L_2$  enters  $A_\alpha$  and  $A_\gamma$ , dividing both of them into three new cells:  $A_\alpha = A_{\alpha\alpha} + A_{\alpha\beta} + A_{\alpha\gamma}$  and  $A_\gamma = A_{\gamma\alpha} + A_{\gamma\beta} + A_{\gamma\gamma}$ , as labeled in Fig. 6. Therefore, future partitions of a cell correspond to the addition of the  $\alpha$ ,

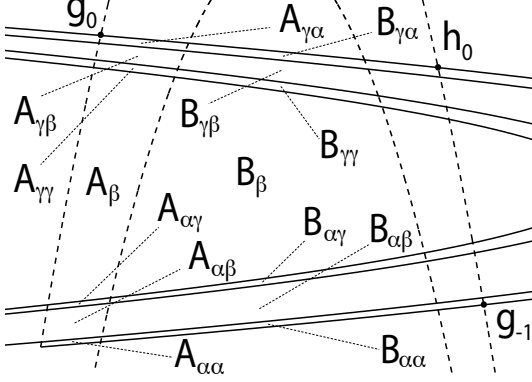


FIG. 6. Zoomed-in graph around the complex region of  $T_{-1,2}$  (same as the lower panel of Fig. 2). The  $A_\alpha$  and  $A_\gamma$  areas in Fig. 5 are partitioned into three sub-areas:  $A_\alpha = A_{\alpha\alpha} + A_{\alpha\beta} + A_{\alpha\gamma}$  and  $A_\gamma = A_{\gamma\alpha} + A_{\gamma\beta} + A_{\gamma\gamma}$ . The  $A_\beta$  area does not get partitioned because of the open system assumption, i.e., manifolds outside of the complex region do not revisit the complex region in future iterations. Since the type-I and type-II cells are always partitioned by any lobe  $L_n$  simultaneously, the  $B_\alpha$  and  $B_\gamma$  cells from Fig. 5 are partitioned in identical ways with  $A_\alpha$  and  $A_\gamma$ , respectively.

$\beta$ , and  $\gamma$  symbols to the end of its existing subscript, except if its subscript ends in  $\beta$  (which terminates that sequence).

In open systems such as the Hénon map, the  $A_\beta$  area does not get partitioned by future iterations because points outside the complex region do not re-enter the complex region, therefore no unstable manifolds will extend inside the lobes  $L_i$  for all  $i \in \mathbb{Z}$ . Since  $A_\beta$  belongs to the inside of  $L_1$ , it will not be partitioned by any future trellises. The same are true for  $A_{\alpha\beta}$ ,  $A_{\gamma\beta}$ , and all areas whose subscript end with  $\beta$  in future trellises, which belong to some future lobes  $L_i$ .

The relative position of the new cells is nontrivial. For example, as shown in Fig. 6,  $A_{\alpha\alpha}$ ,  $A_{\alpha\beta}$ , and  $A_{\alpha\gamma}$  are positioned from the bottom to the top, while  $A_{\gamma\alpha}$ ,  $A_{\gamma\beta}$ ,  $A_{\gamma\gamma}$  are positioned from the top to the bottom, begging the question, how should the order of symbols be assigned for the newly generated cells in a consistent way. The answer is buried in the scaling relations among homoclinic points. As shown in Fig. 7, consider an arbitrary cell area  $A_{\tilde{\omega}}$  in  $T_{-1,n}$ , which is partitioned into three new cells,  $A_{\tilde{\omega}\alpha}$ ,  $A_{\tilde{\omega}\beta}$ , and  $A_{\tilde{\omega}\gamma}$  in  $T_{-1,n+1}$  by lobe  $L_{n+1}$ . Here  $\tilde{\omega}$  denotes a length- $n$  string of symbols composed by arbitrary combinations of  $\alpha$  and  $\gamma$  (but not  $\beta$ ). The middle cell is always labeled by  $\tilde{\omega}\beta$ . Let the four homoclinic points on the corners of this cell be  $a_\beta$ ,  $b_\beta$ ,  $c_\beta$ , and  $d_\beta$ , respectively, all of which belong to  $U_{n+1}$ . The  $\tilde{\omega}\alpha$  subscript is then assigned to the cell with the two corners on

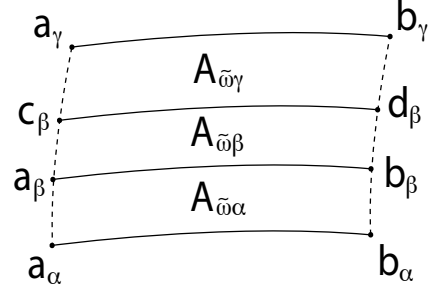


FIG. 7. (Schematic) The cell  $A_{\tilde{\omega}}$  in  $T_{-1,n}$  is partitioned into three new cells in  $T_{-1,n+1}$  by lobe  $L_{n+1}$ :  $A_{\tilde{\omega}} = A_{\tilde{\omega}\alpha} + A_{\tilde{\omega}\beta} + A_{\tilde{\omega}\gamma}$ , where  $A_{\tilde{\omega}\beta} \subset L_{n+1}$ . The rule of assignment is,  $A_{\tilde{\omega}\beta}$  is always assigned to the middle cell, and  $A_{\tilde{\omega}\alpha}$  is assigned to the cell with the two corners, namely  $a_\alpha$  and  $b_\alpha$ , such that  $a_\beta, c_\beta \xrightarrow[k]{S} a_\alpha$  and  $b_\beta, d_\beta \xrightarrow[k]{S} b_\alpha$ , where the order number  $k$  is an appropriate integer that depends on  $\tilde{\omega}$ . Finally,  $A_{\tilde{\omega}\gamma}$  is assigned to the last cell. The same pattern applies to all the  $B$  cells as well.

which  $a_\beta$ ,  $b_\beta$ ,  $c_\beta$ , and  $d_\beta$  accumulate:

$$\begin{aligned} a_\beta, c_\beta &\xrightarrow[k]{S} a_\alpha \\ b_\beta, d_\beta &\xrightarrow[k]{S} b_\alpha. \end{aligned} \quad (26)$$

where the order number  $k$  depends on the detailed forms of  $\tilde{\omega}$ . The  $\tilde{\omega}\gamma$  subscript is assigned to the remaining cell.

For a concrete example, consider the partition  $A = A_\alpha + A_\beta + A_\gamma$  in Fig. 5, where  $A_{\tilde{\omega}} = A$  with  $\tilde{\omega}$  being an empty string. The  $A_\beta$  is first identified as the one in the middle. Notice that its corners,  $g_1, h_1 \xrightarrow[S]{} x$ , and

$a^{(1)}, b^{(1)} \xrightarrow[2]{S} g_{-2}$ , thus  $A_\alpha$  is assigned to the cell at the bottom;  $A_\gamma$  is thus the cell at the top. One can verify that the assignments of cells in Fig. 6 follow the same pattern. In particular, the relative positions of the  $A_{\gamma\alpha}$ ,  $A_{\gamma\beta}$ , and  $A_{\gamma\gamma}$  cells in Fig. 7 are indeed reversed. This can be seen from the zoomed-in Fig. 8, where the four corners of  $A_{\gamma\beta}$ , namely  $v, w, r^{(1)}$ , and  $s^{(1)}$ , accumulate on  $g_0$  and  $b^{(0)}$ :  $v, w \xrightarrow[1]{S} g_0$  and  $r^{(1)}, s^{(1)} \xrightarrow[1]{S} b^{(0)}$ . Thus,  $A_{\gamma\alpha}$  is assigned to the cell on the top of  $A_{\gamma\beta}$ , and  $A_{\gamma\gamma}$  the one at the bottom. The partition of the  $B$  cells follow an identical scheme.

A complete assignment of the areas' symbols are determined by the accumulation relations between homoclinic points along  $S(x)$ , which can be carried on with increasing iterations of  $T_{-1,n}$  to obtain ever finer partitions of type-I and type-II cell areas. The progressive partitioning of the type-I cells can be represented by a *partition tree* shown in Fig. 9. Defining the node  $A$  to be the 0th level of the tree, which is a cell generated by  $T_{-1,0}$ , then nodes at the  $n$ th level along the tree represent the cells newly generated by  $T_{-1,n}$ . Notice the  $\beta$  nodes do not get expanded at the next level, because of the open system



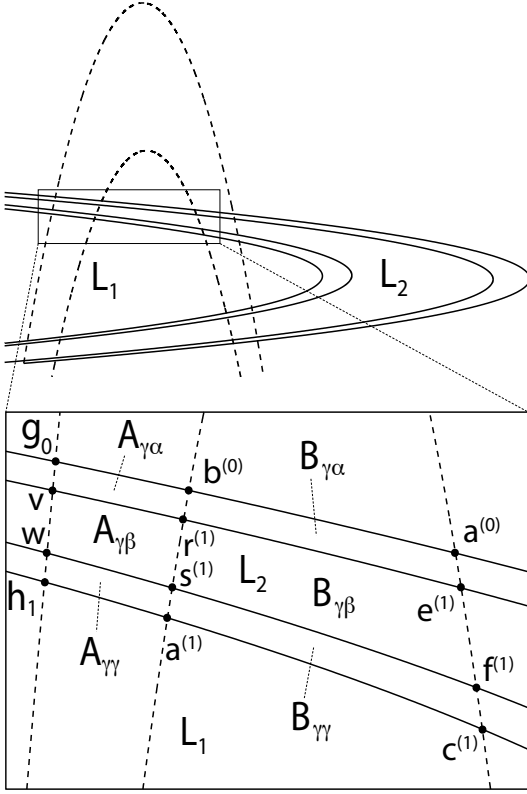


FIG. 8. (Zoomed-in graph) The  $A_\gamma$  and  $B_\gamma$  cells from Fig. 5 are partitioned by  $L_2$  into three new cells each. The  $A_{\gamma\beta}$  area is assigned to the middle one. Since  $v, w \xrightarrow{1_S} g_0$  and  $r^{(1)}, s^{(1)} \xrightarrow{1_S} b^{(0)}$ ,  $A_{\gamma\alpha}$  is assigned to the top one, leaving  $A_{\gamma\gamma}$  to be the bottom one. The same rules apply to the  $B$  cells as well.

assumption. A finite truncation of the partition tree to the  $n$ th level corresponds to the partition of the type-I areas up to  $T_{-1,n}$ . Note that the partition tree of type-II cell areas is identical with the type-I tree upon changing the symbols  $A$  into  $B$ .

#### D. Fast and slow scaling relations

The complete and exact decomposition of the homoclinic orbit actions requires only the areas of the partition trees. On the other hand, their areas scale down asymptotically with the tree level exponentially. Thus, for a desired degree of precision, there exists a level on the tree for which all the areas there and below are negligible for the calculation of orbit actions; the consequences are addressed in Sec. IV C.

The Lyapunov exponent  $\mu$  characterizes the mean stretching and compressing rates along the unstable and stable manifolds, respectively, and therefore governs the typical shrinking rate of cell along the trees. However, it has already been shown that within certain families

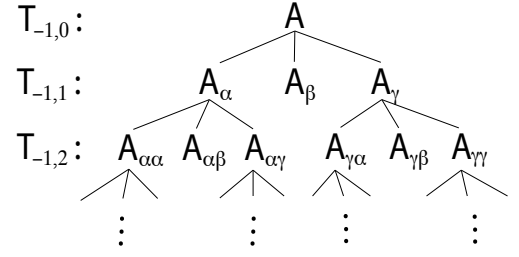


FIG. 9. The partition tree of type-I cell areas. Nodes at the  $n$ th level along the tree are areas generated from the partition of  $T_{-1,n-1}$  by  $T_{-1,n}$ . Every  $\alpha$  and  $\gamma$  nodes are partitioned into three new nodes at the next level, while the  $\beta$  nodes do not get partitioned any further. The partition tree of type-II areas follows an identical pattern upon changing the symbols  $A$  into  $B$ . To order the cells as in the trellis, proceeding from the top of the tree, reverse the order for the next level down each time the number of  $\gamma$  symbols is odd.

there is a faster decay than that. In fact, there are two exponents depending on how one moves within the tree structure. The larger exponent, or fast scaling, applies in the “ $\alpha$ ”-direction, i.e.

$$e^{\mu_x} = \lim_{n \rightarrow \infty} \frac{A_{\tilde{\omega}\alpha^n}}{A_{\tilde{\omega}\alpha^{n+1}}} = \lim_{n \rightarrow \infty} \frac{A_{\tilde{\omega}\alpha^{n-1}\beta}}{A_{\tilde{\omega}\alpha^n\beta}} = \lim_{n \rightarrow \infty} \frac{A_{\tilde{\omega}\alpha^{n-1}\gamma}}{A_{\tilde{\omega}\alpha^n\gamma}}, \quad (27)$$

where  $\alpha^n$  denotes  $n$  consecutive  $\alpha$  characters in the string. The scaling exponent is the same as in Eqs. (21) and (22). Figure 10 illustrates that the three families of areas  $[A_{\tilde{\omega}\alpha^n}]$ ,  $[A_{\tilde{\omega}\alpha^{n-1}\beta}]$ , and  $[A_{\tilde{\omega}\alpha^{n-1}\gamma}]$  ( $n \geq 2$ ) accumulate on  $U[a_\alpha, b_\alpha]$  in the same sense as Eqs. (21) and (22). Starting from the  $A_{\tilde{\omega}}$  cell in  $T_{-1,n}$  and mapping to higher iterations, the addition of  $L_{n+m}$  ( $m = 1, 2, \dots$ ) partitions  $A_{\tilde{\omega}\alpha^{m-1}}$  into three new areas:  $A_{\tilde{\omega}\alpha^m}$ ,  $A_{\tilde{\omega}\alpha^{m-1}\beta}$ , and  $A_{\tilde{\omega}\alpha^{m-1}\gamma}$ , which approach the  $U[a_\alpha, b_\alpha]$  segment asymptotically. The two sequences of points  $[a_{\alpha^{m-1}\beta}]$  and  $[c_{\alpha^{m-1}\beta}]$  ( $m \geq 1$ ), which are created from successive intersections between  $U_{n+m}$  and  $S[a_\alpha, a_\gamma]$ , give rise to two families of points that accumulate on the base point  $a_\alpha$ :

$$a_{\alpha^{m-1}\beta}, c_{\alpha^{m-1}\beta} \xrightarrow[k+m-1]{S} a_\alpha \quad (28)$$

with exponent  $\mu_x$ , where  $k$  depends on the detailed form of  $\tilde{\omega}$ . Similarly, the two sequences of points  $[b_{\alpha^{m-1}\beta}]$  and  $[d_{\alpha^{m-1}\beta}]$  ( $m \geq 1$ ), generated from successive intersections between  $U_{n+m}$  and  $S[b_\alpha, b_\gamma]$ , give rise to two families of points that accumulate on the base point  $b_\alpha$ :

$$b_{\alpha^{m-1}\beta}, d_{\alpha^{m-1}\beta} \xrightarrow[k+m-1]{S} b_\alpha \quad (29)$$

with the same exponent  $\mu_x$  as well. Again, due to the similarity of type-I and type-II cell areas in every trellis, the refinement of  $B$  cells follow an identical pattern, as well as the scaling relations. Therefore, Eq. (27) holds for type-II areas as well.

For example, the three families of areas  $[\mathcal{A}_{SUSU[g_{-2}, b^{(n)}, d^{(n)}, h_{-1}]}^\circ]$ ,  $[\mathcal{A}_{SUSU[b^{(n)}, a^{(n)}, c^{(n)}, d^{(n)}]}^\circ]$ ,



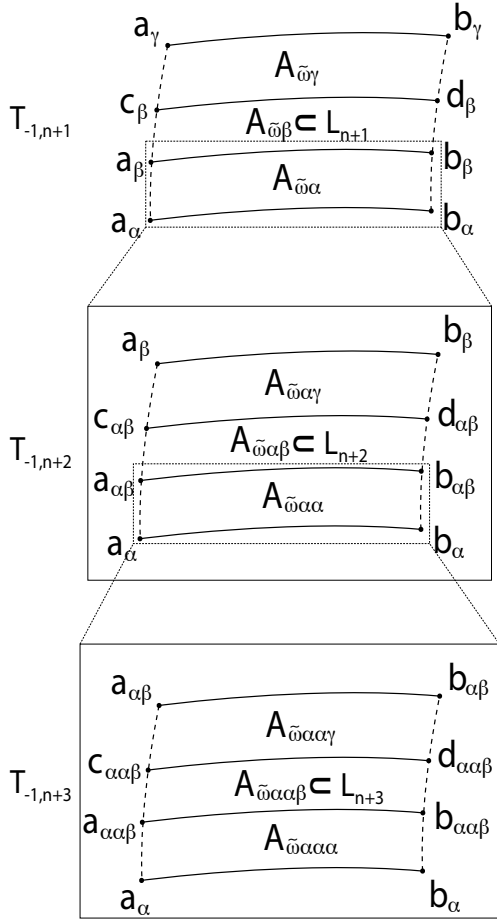


FIG. 10. (Schematic) Successive partitions of  $A_{\tilde{\omega}} \subset T_{-1,n}$  in later trellis  $T_{-1,n+m}$ . Upper panel ( $T_{-1,n+1}$ ): the same as Fig. 7, where  $A_{\tilde{\omega}}$  is partitioned into three areas by  $L_{n+1}$ . Middle panel ( $T_{-1,n+2}$ ): zoomed-in graph of  $A_{\tilde{\omega}\alpha}$  in  $T_{-1,n+2}$ , where  $A_{\tilde{\omega}\alpha}$  is partitioned by  $L_{n+2}$  into three new areas. Lower panel ( $T_{-1,n+3}$ ): zoomed-in graph of  $A_{\tilde{\omega}\alpha\alpha}$  in  $T_{-1,n+3}$ , where  $A_{\tilde{\omega}\alpha\alpha}$  is partitioned by  $L_{n+3}$  into three new areas. The addition of successive lobes create four families of homoclinic points,  $[a_{\alpha^{m-1}\beta}]$ ,  $[c_{\alpha^{m-1}\beta}]$ ,  $[b_{\alpha^{m-1}\beta}]$ , and  $[d_{\alpha^{m-1}\beta}]$ , that accumulate on  $a_{\alpha}$  and  $b_{\alpha}$  under Eqs. (28) and (29) with exponent  $\mu_x$ . Therefore, the three families of areas  $[A_{\tilde{\omega}\alpha^m}]$ ,  $[A_{\tilde{\omega}\alpha^{m-1}\beta}]$ , and  $[A_{\tilde{\omega}\alpha^{m-1}\gamma}]$  also converge onto  $U[a_{\alpha}, b_{\alpha}]$  with exponent  $\mu_x$ , as described by Eq. (27).

and  $[\mathcal{A}_{SUSU[a^{(n)}, b^{(n-1)}, d^{(n-1)}, c^{(n)}]}^{\circ}]$  ( $n \geq 2$ ) from Eq. (21) can be identified as  $[B_{\tilde{\omega}\alpha^n}]$ ,  $[B_{\tilde{\omega}\alpha^{n-1}\beta}]$ , and  $[B_{\tilde{\omega}\alpha^{n-1}\gamma}]$ , respectively, by letting  $\tilde{\omega}$  be an empty string. Comparing the areas in Fig. 2 and Fig. 6, the leading terms in the tree families are identified as  $\mathcal{A}_{SUSU[g_{-2}, b^{(2)}, d^{(2)}, h_{-1}]}^{\circ} = B_{\alpha\alpha}$ ,  $\mathcal{A}_{SUSU[b^{(2)}, a^{(2)}, c^{(2)}, d^{(2)}]}^{\circ} = B_{\alpha\beta}$ , and  $\mathcal{A}_{SUSU[a^{(2)}, b^{(1)}, d^{(1)}, c^{(2)}]}^{\circ} = B_{\alpha\gamma}$ . Although not plotted in the figure, it is easy to visualize conceptually that future lobes partition  $B_{\alpha\alpha}$  into every-finer areas and create the three infinite families of areas that converge to the bottom segment  $U[g_{-2}, h_{-1}]$ .

To check the accuracy of the faster scaling, the first nine areas of the three families  $[A_{\alpha^n}]$ ,  $[A_{\alpha^{n-1}\beta}]$ , and

$[A_{\alpha^{n-1}\gamma}]$  are given in Table I. The three columns give the scaling exponents obtained from  $[A_{\alpha}, A_{\alpha\alpha}, A_{\alpha\alpha\alpha}, \dots]$ ,  $[A_{\beta}, A_{\alpha\beta}, A_{\alpha\alpha\beta}, \dots]$ , and  $[A_{\gamma}, A_{\alpha\gamma}, A_{\alpha\alpha\gamma}, \dots]$ , respectively. Even for the first ratio (worst case), the predicted

n	$\log(\frac{A_{\alpha^n}}{A_{\alpha^{n+1}}})$	$\log(\frac{A_{\alpha^{n-1}\beta}}{A_{\alpha^n\beta}})$	$\log(\frac{A_{\alpha^{n-1}\gamma}}{A_{\alpha^n\gamma}})$
1	2.144099	2.103342	2.197343
2	2.142725	2.142323	2.156467
3	2.142084	2.142521	2.144631
4	2.141952	2.142060	2.142364
5	2.141929	2.141949	2.141991
6	2.141927	2.141929	2.141933
7	2.141892	2.141932	2.141929
8	2.141932	2.141914	2.141718
$\mu_x$	2.141926	2.141926	2.141926

TABLE I. Fast scaling: asymptotic scaling exponents calculated from the Hénon map (Eq. (8) with  $a = 10$ ) using the first nine terms in the three families  $[A_{\alpha^n}]$ ,  $[A_{\alpha^{n-1}\beta}]$ , and  $[A_{\alpha^{n-1}\gamma}]$ .

exponent is good to better than two decimal places. By the bottom of each column, the distinction first appears only in the sixth digit.

The opposite direction down the tree follows increasing repetitions of  $\gamma$  leading to the families,  $[A_{\tilde{\omega}\gamma^{n-1}\alpha}]$ ,  $[A_{\tilde{\omega}\gamma^{n-1}\beta}]$ , and  $[A_{\tilde{\omega}\gamma^n}]$  ( $n \geq 1$ ), respectively. The exponential shrinking rate is much slower, and gives the slow scaling exponent, denoted by  $\mu_s$ :

$$e^{\mu_s} = \lim_{n \rightarrow \infty} \frac{A_{\tilde{\omega}\gamma^{n-1}\alpha}}{A_{\tilde{\omega}\gamma^n\alpha}} = \lim_{n \rightarrow \infty} \frac{A_{\tilde{\omega}\gamma^{n-1}\beta}}{A_{\tilde{\omega}\gamma^n\beta}} = \lim_{n \rightarrow \infty} \frac{A_{\tilde{\omega}\gamma^n}}{A_{\tilde{\omega}\gamma^{n+1}}} \quad (30)$$

which is in complete analogy to Eq. (27), except for a different direction along the tree, and with a different scaling exponent. Unlike the case of Eq. (27), the origin of  $\mu_s$  is still unclear to us. However, as shown by Table II, numerically  $\mu_s$  converges to the value  $\sim 1.48$ . The same

n	$\log(\frac{A_{\gamma^{n-1}\alpha}}{A_{\gamma^n\alpha}})$	$\log(\frac{A_{\gamma^{n-1}\beta}}{A_{\gamma^n\beta}})$	$\log(\frac{A_{\gamma^n}}{A_{\gamma^{n+1}}})$
1	1.320085	2.365152	1.468471
2	1.707766	1.384612	1.446403
3	1.343392	1.460855	1.500372
4	1.535619	1.496668	1.477362
5	1.467206	1.478053	1.484760
6	1.487618	1.484611	1.482549
7	1.481780	1.482579	1.483168
8	1.483367	1.483164	1.482999

TABLE II. Slow scaling: asymptotic scaling exponents calculated from the Hénon map (Eq. (8) with  $a = 10$ ) using the first nine terms in the three families  $[A_{\gamma^{n-1}\alpha}]$ ,  $[A_{\gamma^{n-1}\beta}]$ , and  $[A_{\gamma^n}]$ . After initial fluctuations, the exponents converge to a value around  $\mu_s \sim 1.48$ .

exponent has been verified by choosing a different set of three families,  $[A_{\alpha\gamma^{n-1}\alpha}]$ ,  $[A_{\alpha\gamma^{n-1}\beta}]$ , and  $[A_{\alpha\gamma^n}]$ , as



shown in Table III.  $\mu_s$  is referred to as the slow scaling exponent since it is smaller than  $\mu_x$ .

$n$	$\log(\frac{A_{\alpha\gamma^{n-1}\alpha}}{A_{\alpha\gamma^n\alpha}})$	$\log(\frac{A_{\alpha\gamma^{n-1}\beta}}{A_{\alpha\gamma^n\beta}})$	$\log(\frac{A_{\alpha\gamma^n}}{A_{\alpha\gamma^{n+1}}})$
1	1.364533	2.471588	1.449553
2	1.703491	1.352048	1.444654
3	1.332763	1.460781	1.502057
4	1.541193	1.497815	1.476780
5	1.465512	1.477561	1.484950
6	1.488134	1.484780	1.482495
7	1.481634	1.482527	1.483189

TABLE III. Slow scaling: asymptotic scaling exponents calculated from the Hénon map (Eq. (8) with  $a = 10$ ) using the first eight terms in the three families  $[A_{\alpha\gamma^{n-1}\alpha}]$ ,  $[A_{\alpha\gamma^{n-1}\beta}]$ , and  $[A_{\alpha\gamma^n}]$ . Clearly, these families yield the same exponent  $\mu_s \sim 1.48$  as Table II.

Thus, it appears that the area decays with deepening levels in the partition trees are bounded by two exponents,  $\mu_x$  and  $\mu_s$ , corresponding to the maximum and minimum scaling rates, respectively. The average scaling rate must be characterized by the Lyapunov exponent  $\mu$ , which should lie in the interval  $\mu_s < \mu < \mu_x$ . The rough estimate for the order of magnitude decrease for a cell area  $A_{\tilde{\omega}}$  and  $B_{\tilde{\omega}}$  on the  $N^{th}$  level of the partition trees of  $T_{-1,N}$  is  $\sim O(e^{-\mu N})$ . For a given desired precision in the calculation of homoclinic orbit actions, using the smaller exponent  $\mu_s$  gives the most conservative estimate.

#### IV. HOMOCLINIC ACTION FORMULAS

All the tools are now in place to develop exact relations expressing the classical actions of any homoclinic orbit in  $T_{-1,N}$  (therefore up to transition time  $N + 1$ ), in terms of the type-I and type-II cell areas of  $T_{-1,N}$ . In this method, the calculation of numerical orbits, which suffers from sensitive dependence on initial errors and unstable in nature, are converted into the calculation of areas bounded by  $S(x)$  and  $U(x)$ , which can be evaluated in stable ways. The exact relations of Sec. IV B are perfectly adapted for the development of approximations in Sec. IV C that make use of the asymptotic scaling relations among the areas, and that leads to approximate expressions for the homoclinic orbit actions in  $T_{-1,N}$  using only the type-I and type-II cell areas from  $T_{-1,d(N)}$ , where  $d(N)$  is an integer much smaller than  $N$ . Consequently, it is possible to express the exponentially increasing set of homoclinic orbit actions using a set of areas that is increasing at a much slower rate (e.g., algebraic or linear).

##### A. Projection operations

The main process leading to the homoclinic action formulas in this section is to express the actions of the ho-

moclinic orbits with large winding numbers in terms of those with small winding numbers, i.e., the decomposition of orbits according to their hierarchical structure. To accomplish this, there are some projection operations to be defined which establish mappings between orbits with different winding numbers.

Given a winding- $n$  ( $n \geq 1$ ) homoclinic point  $y$  and two winding- $(n + 1)$  points  $z$  and  $w$  such that  $z \xrightarrow[k]{S} y$  and  $w \xrightarrow[k]{S} y$  ( $\forall k \geq 1$ ) and  $S[y, w] \subset S[y, z]$ , define the *projection operation along the stable manifold*, denoted by  $P_S$ , to be the mapping that maps  $z$  and  $w$  into the base point  $y$ :

$$P_S(z) = P_S(w) = y. \quad (31)$$

The corresponding operation on the symbolic strings, denoted by  $\pi_S$ , can be readily obtained by working backward from Eq. (A5). Namely, given the symbolic codes of  $z$  and  $w$ , the  $\pi_S$  operation deletes the substrings “110 $^{k-1}$ ” and “100 $^{k-1}$ ”, respectively, from the left ends of the cores of  $z$  and  $w$ , while maintaining the position of the decimal point relative to the right end of the core. The resulting symbolic code is then  $y$ . Take the points  $a^{(0)} \Rightarrow \bar{0}1.11\bar{0}$ ,  $b^{(0)} \Rightarrow \bar{0}1.01\bar{0}$  and  $g_{-2} \Rightarrow \bar{0}.01\bar{0}$  in Fig. 13 as examples, we know  $a^{(0)}, b^{(0)} \xrightarrow[1]{S} g_{-2}$ , thus  $P_S(a^{(0)}) = P_S(b^{(0)}) = g_{-2}$ . Correspondingly for the symbolic codes

$$\begin{aligned} \pi_S(\bar{0}1.11\bar{0}) &= \bar{0}.01\bar{0} \\ \pi_S(\bar{0}1.01\bar{0}) &= \bar{0}.01\bar{0} \end{aligned} \quad (32)$$

where the  $\pi_S$  operation deletes either the “11” (for  $a^{(0)}$ ) or “10” (for  $b^{(0)}$ ) substring from the left of the cores while keeping the position of the decimal points relative to the right end of the core unchanged.

Similar operations can be defined for the accumulating homoclinic families along the unstable manifold under the inverse mappings as well. Given a winding- $n$  homoclinic point  $y'$ , and the winding- $(n + 1)$  points  $z'$  and  $w'$  such that  $z' \xrightarrow[k]{U} y'$  and  $w' \xrightarrow[k]{U} y'$  and  $U[y', w'] \subset U[y', z']$ , define the *projection operation along the unstable manifold*, denoted by  $P_U$ , to be the mapping:

$$P_U(z') = P_U(w') = y'. \quad (33)$$

The corresponding operation  $\pi_U$  on the symbolic codes is then defined by working backward from Eq. (A6). Namely, given the symbolic codes of  $z'$  and  $w'$ , the  $\pi_U$  operation deletes the substrings “0 $^{k-1}$ 11” and “0 $^{k-1}$ 01”, respectively, from the right ends of the cores of  $z'$  and  $w'$ , while maintaining the position of the decimal point relative to the left end of the core. The resulting symbolic code then gives  $y'$ .

In the preceding definitions, the projection operations must be applied to homoclinic points with winding numbers  $\geq 2$ . However, they can be naturally extended to



apply to the primary (winding-1) points as well. The extension is straightforward: for any primary homoclinic point  $g_i$  or  $h_i$ , define

$$P_S(g_i) = P_U(g_i) = P_S(h_i) = P_U(h_i) = x \quad (34)$$

with corresponding  $\pi_S$  and  $\pi_U$  operations mapping the symbolic codes of  $h_i$  and  $g_i$  into  $\bar{0}.\bar{0}$ , i.e., that of the hyperbolic fixed point  $x$ . This is consistent with the scaling relations of Eqs. (24) and (25) as well.

Since  $\pi_S$  and  $\pi_U$  operate on different sides of the cores, it is easy to see that they commute:  $\pi_S\pi_U = \pi_U\pi_S$ . Since the symbolic codes are in one-to-one correspondences with the phase space points, the projection operations  $P_S$  and  $P_U$  also commute:  $P_S P_U = P_U P_S$ . Therefore, a mixed string of operations consisting of  $n$  applications of  $P_S$  and  $m$  applications of  $P_U$ , disregarding their relative orders, can always be written as  $P_S^n P_U^m$ , and similarly for the mixed string of operations of  $\pi_S$  and  $\pi_U$  as well. Such operations are extensively used in the decomposition scheme in Sec. IV B.

As an example, consider the  $c^{(1)} \Rightarrow \bar{0}11.11\bar{0}$ ,  $h_{-1} \Rightarrow \bar{0}.11\bar{0}$ , and  $h_1 \Rightarrow \bar{0}11.\bar{0}$  points from Fig. 13. The accumulation relations are  $c^{(1)} \xrightarrow[S]{1} h_{-1} \xrightarrow[U]{\hookrightarrow} x$  and  $c^{(1)} \xrightarrow[U]{1} h_1 \xrightarrow[S]{\hookrightarrow} x$ , thus  $P_U P_S(c^{(1)}) = P_U(h_{-1}) = x$  and  $P_S P_U(c^{(1)}) = P_S(h_1) = x$ . On the other hand, using the symbolic dynamics we have  $\pi_U \pi_S(\bar{0}11.11\bar{0}) = \pi_U(\bar{0}.11\bar{0}) = \bar{0}.\bar{0}$  and  $\pi_S \pi_U(\bar{0}11.11\bar{0}) = \pi_S(\bar{0}11.\bar{0}) = \bar{0}.\bar{0}$ , consistent with the results from the accumulation relations.

## B. Exact decomposition

The derivation of the exact formula makes repeated use of the MacKay-Meiss-Percival action principle described by Eqs. (13) and (14), and expresses the relative classical actions of homoclinic orbits as sums of phase-space areas bounded by  $S(x)$  and  $U(x)$ . The fixed point orbit  $\{x\}$  becomes a natural candidate for a reference orbit, and the actions of all homoclinic orbits  $\{h\}$  can be expressed relative to  $\{x\}$  in the form of  $\Delta\mathcal{F}_{\{h\}\{x\}}$ , as shown by Eq. (14).

Start by calculating the actions of the two primary orbits  $\{g_0\}$  and  $\{h_0\}$ , which readily follow from Eq. (14). The two areas  $\mathcal{A}_{US[x,h_0]}^\circ$  and  $\mathcal{A}_{US[x,g_0]}^\circ$  are straightforward to evaluate since only short segments of  $S(x)$  and  $U(x)$  are required. Having the primary relative orbit actions available, the actions of all winding- $n$  orbits ( $n \geq 2$ ) can be determined recursively from the actions of the winding- $(n-1)$  and winding- $(n-2)$  orbits. In particular, given any winding- $n$  ( $n \geq 2$ ) homoclinic point  $y \in S_{-1} \cap U_m$ , the action of  $\{y\}$  can be expressed using three auxiliary orbits:  $\{P_S(y)\}$ ,  $\{P_U(y)\}$ , and  $\{P_S P_U(y)\}$ . Substituting  $\{y\}$ ,  $\{P_U(y)\}$ ,  $\{P_S(y)\}$ ,

and  $\{P_S P_U(y)\}$  into Eq. (15) gives

$$\begin{aligned} & (\Delta\mathcal{F}_{\{y\}\{x\}} - \Delta\mathcal{F}_{\{P_U(y)\}\{x\}}) \\ & - (\Delta\mathcal{F}_{\{P_S(y)\}\{x\}} - \Delta\mathcal{F}_{\{P_S P_U(y)\}\{x\}}) \\ & = \mathcal{A}_{SU SU[y, P_S(y), P_S P_U(y), P_U(y)]}^\circ \end{aligned} \quad (35)$$

and therefore

$$\begin{aligned} \Delta\mathcal{F}_{\{y\}\{x\}} &= \Delta\mathcal{F}_{\{P_S(y)\}\{x\}} + \Delta\mathcal{F}_{\{P_U(y)\}\{x\}} \\ & - \Delta\mathcal{F}_{\{P_S P_U(y)\}\{x\}} + \mathcal{A}_{SU SU[y, P_S(y), P_S P_U(y), P_U(y)]}^\circ. \end{aligned} \quad (36)$$

Notice that the  $P_S$  and  $P_U$  operations reduce the winding number of  $y$  by 1. Similarly, from Eqs. (A5) and (A6) the core length is reduced by at least 2, since their effect is to delete substrings of a minimum of two digits from the original core (“110<sup>k-1</sup>” or “100<sup>k-1</sup>” for  $P_S$ , “0<sup>k-1</sup>11” or “0<sup>k-1</sup>01” for  $P_U$ ). Therefore, the three auxiliary orbits are guaranteed to have simpler and shorter phase-space excursions than  $\{y\}$ . In this sense, Eq. (36) provides a decomposition of the relative action of any arbitrary homoclinic orbit into the relative actions of three simpler auxiliary homoclinic orbits, plus a phase-space area bounded by the manifolds. By repeated contractions, the decomposition could be pushed to involving only the primary homoclinic orbits, the fixed point, and a set of areas. Implied by this process is that the inverse sequences could be used beginning with the two primary homoclinic orbits, fixed point, and a set of areas to construct the relative actions of all the homoclinic orbits.

An important outcome, buried in Eq. (36), relates to the particular form of  $\mathcal{A}_{SU SU[y, P_S(y), P_S P_U(y), P_U(y)]}^\circ$ . For any  $y \in S_{-1} \cap U_m$ , the locations of its projections are highly constrained:  $P_S(y) \in S_{-1}$ ,  $P_U(y) \in S[x, g_0]$ , and  $P_S P_U(y) \in S[x, g_0]$ . As a consequence,  $\mathcal{A}_{SU SU[y, P_S(y), P_S P_U(y), P_U(y)]}^\circ$  is always expressible by the type-I and -II cell areas of  $T_{-1,m}$ . Consider  $c^{(1)} \in (S_{-1} \cap U_1)$  from Fig. 13 for example, the use of Eq. (36) yields:

$$\begin{aligned} \Delta\mathcal{F}_{\{c^{(1)}\}\{x\}} &= \Delta\mathcal{F}_{\{h_{-1}\}\{x\}} + \Delta\mathcal{F}_{\{h_1\}\{x\}} \\ & - \Delta\mathcal{F}_{\{x\}\{x\}} + \mathcal{A}_{SU SU[c^{(1)}, h_{-1}, x, h_1]}^\circ \end{aligned} \quad (37)$$

where  $\Delta\mathcal{F}_{\{x\}\{x\}} = 0$  gives zero contributions. Comparing Fig. 13 with Fig. 5, the  $\mathcal{A}_{SU SU[c^{(1)}, h_{-1}, x, h_1]}^\circ$  term is expressible by four cell areas from the type-I and type-II partition trees of  $T_{-1,1}$ :

$$\mathcal{A}_{SU SU[c^{(1)}, h_{-1}, x, h_1]}^\circ = A_\alpha + A_\beta + B_\alpha + B_\beta \quad (38)$$

all of which are finite curvy trapezoids bounded by the manifolds that can be evaluated simply. The same results hold for all homoclinic points on  $S_{-1}$  with a single exception— $a^{(0)}$ . The use of Eq. (36) on  $a^{(0)}$  gives

$$\begin{aligned} \Delta\mathcal{F}_{\{a^{(0)}\}\{x\}} &= \Delta\mathcal{F}_{\{g_{-2}\}\{x\}} + \Delta\mathcal{F}_{\{g_0\}\{x\}} \\ & + \mathcal{A}_{SU SU[a^{(0)}, g_{-2}, x, g_0]}^\circ \end{aligned} \quad (39)$$



where the evaluation of  $\mathcal{A}_{SU[SU[a^{(0)}, g_{-2}, x, g_0]]}^\circ$  (Fig. 13) requires the additional area  $\mathcal{A}_{SU[a^{(0)}, b^{(0)}]}^\circ$  that is not part of the partition tree areas. Although the calculation of  $\mathcal{A}_{SU[a^{(0)}, b^{(0)}]}^\circ$  is not difficult, to make the scheme consistent for all homoclinic points, an alternate form of Eq. (36) is used:

$$\Delta\mathcal{F}_{\{a^{(0)}\}\{x\}} = \Delta\mathcal{F}_{\{h_{-1}\}\{x\}} + \Delta\mathcal{F}_{\{g_0\}\{x\}} + \mathcal{A}_{SU[SU[a^{(0)}, h_{-1}, x, g_0]]}^\circ \quad (40)$$

so  $\mathcal{A}_{SU[SU[a^{(0)}, h_{-1}, x, g_0]]}^\circ$  is expressible by cell areas  $A + B$ .

Although  $\mathcal{A}_{SU[SU[y, P_S(y), P_S P_U(y), P_U(y)]]}^\circ$  is expressible by linear combinations of type-I and type-II partition tree areas,  $A_\omega$ , the precise mapping between this area and the tree area symbols must be determined. Given the symbolic code of any homoclinic point  $y \in (S_{-1} \cap U_m)$ , the explicit mapping links  $\mathcal{A}_{SU[SU[y, P_S(y), P_S P_U(y), P_U(y)]]}^\circ$  with specific linear combinations of cell areas from the type-I and type-II partition trees of  $T_{-1, m}$ . Since the transition time of  $y$  is  $m + 1$ , according to Eq. (A2), its core length is  $m + 3$ . Let  $\tilde{\gamma} = s_1 s_2 \cdots s_{m+2} s_{m+3}$  ( $s_i \in \{0, 1\}$ ,  $s_1 = s_{m+3} = 1$ ) be the core of the symbolic code of  $y$ , then the linear combination of cell areas depends solely on  $\tilde{\gamma}$ . As the association is rather technical, the details are given in App. C. The correspondence is given by Eq. (C4) using the notation and other relations also defined in the appendix.

Even though the actions of individual homoclinic orbits can always be calculated directly with the MacKay-Meiss-Percival action principle:  $\Delta\mathcal{F}_{\{y\}\{x\}} = \mathcal{A}_{US[x, y]}^\circ$ , for those orbits with large transit times, the integration path  $US[x, y]$  will be stretched exponentially long and extend far from the fixed point. Accurate interpolation of the path will require an exponentially growing set of points on the manifolds to maintain a reasonable density, an impractical task given the formidable computation time and memory space. On the other hand, using Eqs. (36) and (C4), the entire set of the homoclinic orbit actions arising from any trellis  $T_{-1, N}$ , can be calculated with the two primary orbit actions,  $\Delta\mathcal{F}_{\{h_0\}\{x\}}$  and  $\Delta\mathcal{F}_{\{g_0\}\{x\}}$ , and the areas of the cells of the type-I and type-II partition trees of  $T_{-1, N}$ . These areas are confined to a finite region of the phase space, and bounded by stable and unstable manifolds with small curvatures, which are far easier to compute. Notice that both the symbolic codes of homoclinic points and the numerical areas in the partition trees can be generated with straightforward computer algorithms, so the recursive use of Eqs. (36) and (C4) give rise to an automated computational scheme for the exact calculation of homoclinic orbit actions.

Equivalently, one may carry out the recursive process explicitly, which leads to an expression of the homoclinic orbit action as a cell-area expansion. This is done by expanding the three auxiliary homoclinic orbit actions in Eq. (36) using the equation itself, repeatedly, until all auxiliary orbits reduce to the primary homo-

clinic orbits. However, there is a technical difficulty of Eq. (36) to take into account: the point  $P_U(y)$  is no longer on  $S_{-1}$ , so the area term in its own expansion,  $\mathcal{A}_{SU[SU[P_U(y), P_S P_U(y), P_S P_U^2(y), P_U^2(y)]]}^\circ$ , is no longer being expressed by the type-I and type-II cell areas. Consequently, Eq. (C4) breaks down for  $P_U(y)$ . The same is true for point  $P_S P_U(y)$  as well. To adjust for this problem, all that is needed is to identify the representative point of the orbit  $\{P_U(y)\}$  on  $S_{-1}$ , denoted by  $P'_U(y)$ . In fact,  $P'_U(y)$  is just an image of  $P_U(y)$  under several inverse mappings. The number of inverse mappings is straightforwardly identified. All homoclinic points on  $S_{-1}$  have symbolic codes of the form  $0\tilde{\zeta}.010\bar{0}$  (if they are located on  $S[b^{(0)}, g_{-2}]$ ) or  $0\tilde{\zeta}.110\bar{0}$  (if they are located on  $S[h_{-1}, a^{(0)}]$ ), where  $\tilde{\zeta}$  denotes an arbitrary symbolic string of binary digits. Thus, the decimal point of the symbolic code of any homoclinic point on  $S_{-1}$  is always two digits left of the right end of its core. Hence, the resultant shift of the decimal point of  $P_U(y)$  yields  $P'_U(y)$ . Suppose the decimal point of  $P_U(y)$  is  $n'$  digits to the right side of the right end of its core, then the  $P'_U$  operation can be defined as

$$P'_U(y) = M^{-(n'+2)} P_U(y). \quad (41)$$

The corresponding symbolic operation  $\pi'_U$  can be defined as a shift of the decimal point for  $n' + 2$  digits towards the left, after the operation  $\pi_U$ .

For the special cases of  $y = h_i$  or  $y = g_i$ , i.e., a primary homoclinic point,  $P_U(y)$  reduces to  $x$ , and  $n'$  loses its meaning. For those cases, define

$$P'_U(h_i) = P'_U(g_i) = x \quad (42)$$

and the corresponding  $\pi'_U$  operation maps the symbolic codes of the primary homoclinic points into  $0.0$ , i.e., that of the hyperbolic fixed point.

The commutative relations hold for both the projection operations and their symbolic counterparts:  $P_S P'_U = P'_U P_S$  and  $\pi_S \pi'_U = \pi'_U \pi_S$ . Using the  $P'_U$  operation, Eq. (36) can be written alternatively as

$$\Delta\mathcal{F}_{\{y\}\{x\}} = \Delta\mathcal{F}_{\{P_S(y)\}\{x\}} + \Delta\mathcal{F}_{\{P'_U(y)\}\{x\}} - \Delta\mathcal{F}_{\{P_S P'_U(y)\}\{x\}} + \mathcal{A}_{SU[SU[y, P_S(y), P_S P_U(y), P_U(y)]]}^\circ, \quad (43)$$

in which the representative points  $P'_U(y)$  and  $P_S P'_U(y)$  of the auxiliary homoclinic orbits  $\{P'_U(y)\}$  and  $\{P_S P'_U(y)\}$  both locate on  $S_{-1}$  now. Therefore, the recursive expansion of Eq. (43) can be continued until all auxiliary orbits involved are primary homoclinic orbits.

Consider the case of  $\{y\}$  with winding-2. Then  $P_S P_U(y) = x$ , thus  $\Delta\mathcal{F}_{\{P_S P_U(y)\}\{x\}} = 0$ . The two non-vanishing auxiliary orbits are  $\{P_S(y)\}$  and  $\{P'_U(y)\}$ , both of which are primary orbits, so Eq. (43) is already a complete expansion. For all higher winding cases,  $n \geq 3$ , it is possible to expand the  $\Delta\mathcal{F}_{\{P_S(y)\}\{x\}}$  and  $\Delta\mathcal{F}_{\{P'_U(y)\}\{x\}}$  terms in Eq. (43) using the equation itself to obtain a twice-iterated formula



$$\begin{aligned} \Delta\mathcal{F}_{\{y\}\{x\}} &= \Delta\mathcal{F}_{\{P_S^2(y)\}\{x\}} + \Delta\mathcal{F}_{\{P_S P'_U(y)\}\{x\}} + \Delta\mathcal{F}_{\{P_U^2(y)\}\{x\}} - \Delta\mathcal{F}_{\{P_S^2 P'_U(y)\}\{x\}} - \Delta\mathcal{F}_{\{P_S P_U^2(y)\}\{x\}} \\ &+ \mathcal{A}_{SUSU[y, P_S(y), P_S P_U(y), P_U(y)]}^\circ + \mathcal{A}_{SUSU[P_S(y), P_S^2(y), P_S^2 P_U(y), P_S P_U(y)]}^\circ + \mathcal{A}_{SUSU[P'_U(y), P_S P'_U(y), P_S P_U P'_U(y), P_U P'_U(y)]}^\circ. \end{aligned} \quad (44)$$

Since  $y$ ,  $P_S(y)$ , and  $P'_U(y)$  are all located on  $S_{-1}$ , with the help of Eq. (C4), the three  $\mathcal{A}_{SUSU[\dots]}^\circ$  areas in the above formula are all expressible using type-I and type-II areas. For the orbits with  $n = 3$ , both  $\Delta\mathcal{F}_{\{P_S^2 P'_U(y)\}\{x\}}$  and  $\Delta\mathcal{F}_{\{P_S P_U^2(y)\}\{x\}}$  vanish, so no more expansions are needed. For the  $n \geq 4$  cases, the above procedure can be carried on repeatedly, until the  $P_S^{n-i} P_U^i(y)$  ( $1 \leq i \leq n-1$ ) action terms are present, which reduce  $y$  into  $x$ . Therefore, a general formula for the complete action decomposition of any winding- $n$  homoclinic orbit  $\{y\}$  (where  $y \in S_{-1} \cap U_m$ ) can be written as

$$\Delta\mathcal{F}_{\{y\}\{x\}} = \sum_{i=0}^{n-1} \Delta\mathcal{F}_{\{P_S^{n-1-i} P_U^i(y)\}\{x\}} + \sum_{i=0}^{n-2} \sum_{j=0}^i \mathcal{A}_{SUSU[P_S^{i-j} P_U^j(y), P_S^{i-j+1} P_U^j(y), P_S^{i-j+1} P_U P_U^j(y), P_S^{i-j} P_U P_U^j(y)]}^\circ. \quad (45)$$

where the  $\Delta\mathcal{F}_{\{P_S^{n-1-i} P_U^i(y)\}\{x\}}$  terms are relative actions of the primary homoclinic orbits, therefore either  $\Delta\mathcal{F}_{\{h_0\}\{x\}}$  or  $\Delta\mathcal{F}_{\{g_0\}\{x\}}$ . The  $\mathcal{A}_{SUSU[\dots]}^\circ$  terms in the double sum are areas of the curvy parallelograms spanned by four homoclinic points of various winding numbers, generated from mixed projections of  $y$ . By design, all  $P_S^{i-j} P_U^j(y)$  points in these areas are located on  $S_{-1}$ , thus the  $\mathcal{A}_{SUSU[\dots]}^\circ$  terms are expressible using the type-I and type-II cells via Eq. (C4).

Eq. (45) gives a complete expansion of the homoclinic orbit actions in terms of the primary homoclinic orbit actions plus the cell areas of type-I and type-II partition trees. It converts the determinations of numerical orbits into area calculations in a finite region of the phase space, and avoids exponentially extending integration paths associated with complicated orbits. Furthermore, the two types of cells come from a nearly parallel and linear foliated phase-space region with relatively small curvature along the manifolds, so the numerical interpolation of the manifolds does not require a very dense set of points, and therefore renders the calculations practical.

Nevertheless, the total number of the cell areas proliferates with the same rate as the homoclinic points on  $S_{-1}$ . This is because the cells can be put into an one-to-one correspondence with the non-primary homoclinic points on  $S_{-1}$ , such that each cell corresponds to the homoclinic point at its upper right corner. For example, in Fig. 5, the cells  $A_\alpha, A_\beta, A_\gamma, B_\alpha, B_\beta$ , and  $B_\gamma$  correspond to points  $b^{(1)}, a^{(1)}, b^{(0)}, d^{(1)}, c^{(1)}$ , and  $a^{(0)}$ , respectively. As we increase the integer  $N$  of the trellis  $T_{-1,N}$ , new cells emerge at an identical rate with new homoclinic points on  $S_{-1}$ , both of which proliferate as  $2^{N+2} = e^{\alpha(N+2)}$ , where  $\alpha = \log 2$  is the topological entropy of the system. Therefore, the exact evaluation of homoclinic orbit actions, Eq. (45) requires an exponentially increasing set of areas for its input, as must happen.

### C. Information reduction

In semiclassical approximations, the classical actions divided by  $\hbar$  determine phase angles, and as it is already an approximation to begin with, it is possible to tolerate small errors, say  $\epsilon = \delta\mathcal{F}/\hbar$ , measured in radians. As a practical matter, once this ratio is  $\lesssim 0.1$  or some similar scale, constructive and destructive interferences are properly predicted, and much greater precision becomes increasingly irrelevant. Given that the areas in Eq. (45), or similarly of the partition tree cells, shrink exponentially rapidly most of these corrections can be dropped or ignored.

Identifying the necessary information begins with an estimate of orders of magnitudes of the areas terms in Eq. (45). Given any trellis  $T_{-1,N}$ , the maximum winding number of a homoclinic orbit is  $n_{\max} = N/2 + 2$ . Due to the slow scaling direction of the tree structure, the orbit  $y \Rightarrow \overline{01}^{N+1}.110$  yields an expansion with the largest possible number of significant  $\mathcal{A}_{SUSU[\dots]}^\circ$  terms, and hence an upper bound on the number of necessary areas.

It is reasonable to assume the cell areas  $A$  and  $B$  of  $T_{-1,0}$  are of the same magnitude, and it is sufficient to consider the ratios  $\mathcal{R}(\mathcal{A}) = \mathcal{A}_{SUSU[\dots]}^\circ/A$ . To simplify notation, let  $y' = P_S^{i-j} P_U^j(y)$ , so the area  $\mathcal{A}_{SUSU[P_S^{i-j} P_U^j(y), P_S^{i-j+1} P_U^j(y), P_S^{i-j+1} P_U P_U^j(y), P_S^{i-j} P_U P_U^j(y)]}^\circ$  is denoted  $\mathcal{A}_{SUSU[y', P_S(y'), P_S P_U(y'), P_U(y')]}^\circ$ , which is expressible as a linear combination of cell areas of partition trees of  $T_{-1,N-2i}$  via Eq. (C4). These cell areas are at the  $(N-2i)$ th level of the partition trees, hence the scaling relation, Eq. (30), gives ratio estimates  $\sim e^{-\mu_s(N-2i)}$ . As a result, the inner area sum of Eq. (45) gives

$$\sum_{j=0}^i \mathcal{A}_{SUSU[P_S^{i-j} P_U^j(y), P_S^{i-j+1} P_U^j(y), P_S^{i-j+1} P_U P_U^j(y), P_S^{i-j} P_U P_U^j(y)]}^\circ \sim AO\left((i+1)e^{-\mu_s(N-2i)}\right). \quad (46)$$



Comparing this estimate with the threshold  $\delta\mathcal{F}$  yields a maximum depth of the tree needed  $d = N - 2i$ :

$$A(i+1)e^{-\mu_s d} \geq \delta\mathcal{F}, \quad (47)$$

therefore

$$e^{-\mu_s d} \geq \frac{\epsilon\hbar}{A(i+1)}. \quad (48)$$

A slightly more conservative bound replaces  $i+1$  with  $n_{max} \approx N/2$  and gives after some algebra

$$d \leq \frac{1}{\mu_s} \log \frac{NA}{2\epsilon\hbar}. \quad (49)$$

Therefore, in order to calculate all homoclinic orbit actions arising from  $T_{-1,N}$  within the error tolerance  $\epsilon\hbar$ , we only need to determine numerically the type-I and type-II cell areas of the partition trees of  $T_{-1,d}$ . Recall that the number of cell areas in  $T_{-1,d}$  is estimated by

$$e^{\alpha d} \sim \left( \frac{NA}{2\epsilon\hbar} \right)^{\frac{\alpha}{\mu_s}}, \quad (50)$$

while the number of homoclinic orbits in  $T_{-1,N}$  is  $\propto e^{\alpha N}$ , where  $\alpha = \log 2$  is the topological entropy of the system.

In practice, the use of  $T_{-1,d}$  to construct the relative actions of  $T_{-1,N}$  alters the area sum in Eq. (45), such that any  $\mathcal{A}_{SU[SU[P_S^{i-j}P_U^{j'}(y), P_S^{i-j+1}P_U^{j'}(y), P_S^{i-j+1}P_U^{j'}(y), P_S^{i-j}P_U^{j'}(y)]}$  terms with  $P_S^{i-j}P_U^{j'}(y) \notin T_{-1,d}$  will be excluded from the double sum, leading to the reduced action formula:

$$\Delta\mathcal{F}_{\{y\}\{x\}} = \sum_{i=0}^{n-1} \Delta\mathcal{F}_{\{P_S^{n-1-i}P_U^{i'}(y)\}\{x\}} + \sum_{i=0}^{n-2} \sum_{j=0}^i \mathcal{A}_{SU[SU[P_S^{i-j}P_U^{j'}(y), P_S^{i-j+1}P_U^{j'}(y), P_S^{i-j+1}P_U^{j'}(y), P_S^{i-j}P_U^{j'}(y)]} + O(\delta\mathcal{F}), \quad (51)$$

where the inner primed sum  $\sum_{j=0}^i$  means a sum with constraint  $P_S^{i-j}P_U^{j'}(y) \in T_{-1,d}$ .

#### D. Numerical example

For the Hénon map in Eq. (8) with  $a = 10$ , and an error tolerance  $\delta\mathcal{F}/A = 0.001$ , the natural logarithmic dependence of  $d$  on  $N$  is shown in Fig. 11. The information reduction is significant: even for the calculation of homoclinic orbit actions of  $T_{-1,100}$ , which is obviously impossible via traditional methods, our scheme only requires the numerical computation of cell areas up to  $T_{-1,8}$ , an effortless task for personal computers.

For the numerical verification of Eqs. (45) and (51), we calculate the relative actions of the homoclinic orbits of  $T_{-1,N}$  in three different ways. The first method is to implement the orbit finder method introduced in our previous work [18], which determines the numerical orbits  $\{y\}$  and thus their relative actions,  $\Delta\mathcal{F}_{\{y\}\{x\}}^{(\text{ref.})}$ . These actions are the standard reference actions for comparison. The second method is to calculate the cell areas in the partition trees of  $T_{-1,N}$ , and evaluate the actions  $\Delta\mathcal{F}_{\{y\}\{x\}}^{(\text{exact})}$  using Eqs. (45) and (C4). These should only differ from  $\Delta\mathcal{F}_{\{y\}\{x\}}^{(\text{ref.})}$  due to relying on double precision computation since both are exact evaluations with no approximations involved. On the contrary, in the third method the tolerance is  $\delta\mathcal{F}/A = 0.001$  (where  $A \approx 10.973$  for the current case of  $a = 10$ ), and only cell areas of the partition trees up to the reduced trellis  $T_{-1,d}$  are used with Eqs. (51)

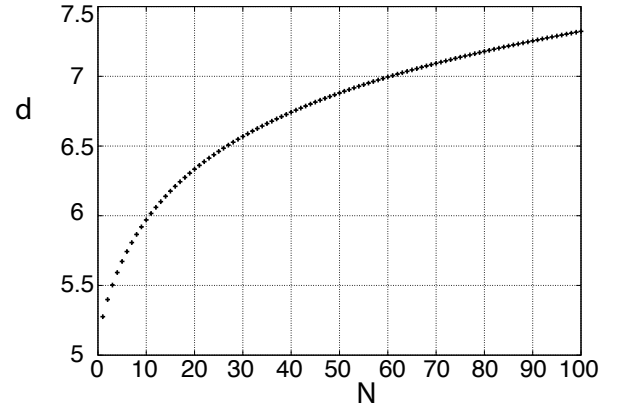


FIG. 11. The logarithmic dependence of  $d$  with respect to  $N$  using the slow scaling exponent  $\mu_s = 1.483$ , error tolerance  $\delta\mathcal{F}/A = 0.001$  and  $a = 10$  for the Hénon map. For the computation of large trellises such as  $N = 100$ , the approximate formula of Eq. (51) only requires the computation of cell areas up to trellis number  $d = 8$ .

and (C4) to obtain the approximate actions,  $\Delta\mathcal{F}_{\{y\}\{x\}}^{(\text{approx.})}$ .

Every homoclinic orbit up to iteration number  $N = 10$  is constructed, which corresponds to trellis  $T_{-1,10}$ . The total number of orbits is  $2^{12} = 4096$ . The reduced iteration number for this case is  $d = 6$ , i.e., the relative homoclinic orbit actions in  $T_{-1,10}$  should be given to an accuracy  $A \times O(10^{-3}) \sim 1 \times 10^{-2}$  or better using only the cell areas from  $T_{-1,6}$ .

Due to the large number of orbits, it is impractical to list the results for  $\Delta\mathcal{F}_{\{y\}\{x\}}^{(\text{exact})}$  and  $\Delta\mathcal{F}_{\{y\}\{x\}}^{(\text{approx.})}$  for ev-



ery orbit. Instead, we show the two orbits that yield the maximum errors. The homoclinic orbit that leads to the maximum error in  $\Delta\mathcal{F}_{\{y\}\{x\}}^{(\text{exact})}$  out of all 4096 orbits is  $\{y\} \Rightarrow \bar{0}1010001100011\bar{0}$ , for which

$$\Delta\mathcal{F}_{\{y\}\{x\}}^{(\text{exact})} - \Delta\mathcal{F}_{\{y\}\{x\}}^{(\text{ref.})} = 8.08 \times 10^{-8}. \quad (52)$$

Compared to the orbit action itself,  $\Delta\mathcal{F}_{\{y\}\{x\}}^{(\text{ref.})} = -466.602\,850\,894\,90$ , the relative error is around  $1.7 \times 10^{-10}$ , almost as good as possible due to the presence of interpolation error. This demonstrates the accuracy of Eq. (45).

As for  $\Delta\mathcal{F}_{\{y\}\{x\}}^{(\text{approx.})}$ , the maximum error emerges for the orbit  $\{y\} \Rightarrow \bar{0}11111111111\bar{0}$ , for which

$$\Delta\mathcal{F}_{\{y\}\{x\}}^{(\text{approx.})} - \Delta\mathcal{F}_{\{y\}\{x\}}^{(\text{ref.})} = -5.453 \times 10^{-3} \quad (53)$$

which is well below the error tolerance  $1 \times 10^{-2}$ . Compared to the orbit action itself,  $\Delta\mathcal{F}_{\{y\}\{x\}}^{(\text{ref.})} = -628.514\,708\,240\,16$ , the relative error is around  $8.7 \times 10^{-6}$ .

## V. CONCLUSIONS

It is possible to construct the complete set of homoclinic orbit relative actions arising from horseshoe-shaped homoclinic tangles in terms of the primitive orbits' relative actions and an exponentially decreasing set of parallelogram-like areas bounded by stable and unstable manifolds. Important constraints exist on the distribution of homoclinic points [38, 59], which are imposed by the topology of the homoclinic tangle. This enables an organizational scheme for the orbits by their winding numbers and assigns binary symbolic codes to each of them. The projection operations,  $P_S$  and  $P_U$ , together with the corresponding symbolic operations,  $\pi_S$  and  $\pi_U$ , link homoclinic points of different winding numbers. Based on a judicious use of the MacKay-Meiss-Percival action principle and mixed projections of all degrees, an exact geometric formula [Eq. (45)] emerges that determines their relative actions in terms of cell areas from a finite region of phase space, which are bounded by manifolds with low curvatures. However, these areas still proliferate at the same rate as the homoclinic points, which become exponentially hard to compute for large iterations numbers  $N$ . To overcome this, we made use of the exponential decay of cell areas in the partition trees, and eliminated all small areas that are asymptotically negligible. The exponentially shrinking areas have their origins in the asymptotic foliations of stable and unstable manifolds, and are thus generic to all chaotic systems. The resulting approximate expression [Eq. (51)] relies on a logarithmically reduced amount of information relative to the exact Eq. (45). It gives the relative actions or orbits in  $T_{-1,N}$  using only the areas from  $T_{-1,d}$ , in exchange for comprising the accuracy by a designated order of magnitude  $O(\delta\mathcal{F} = \epsilon\hbar)$ .

For semiclassical trace formulas, once the actions are determined to within an appropriate tolerance level such as mentioned above, additional accuracy becomes irrelevant and of no consequence. Straightforward computations of the actions rely on the numerical constructions of orbits, for which the difficulties are twofold. First, in highly chaotic systems, numerical determination of individual long orbits suffer from sensitive dependence on initial errors. Second, the total number of orbits proliferates exponentially rapidly with relevant time scales (the trellis number  $N$  in our case). For homoclinic, heteroclinic, and periodic orbits in Hamiltonian chaos with two degrees of freedom, the first difficulty is not fundamental, and solvable in many ways. The second difficulty, addressed in the present article, illustrates in great detail how information entropy vanishes for quantum systems (isolated, bounded, non-measured) from the perspective of semiclassical theory. The reduction of information implied by  $\hbar$  or any error tolerance criterion produces an exponentially increasing set of output calculations using a slower-than-exponentially (i.e., algebraically) increasing set of input information.

This method has the potential to serve as a generic paradigm for the information reduction of semiclassical calculations of chaotic systems. Although the present work is focused on homoclinic orbit actions, the results can be immediately generalized into broader contexts, such as the evaluation of unstable periodic orbit actions. Such connections are made possible by our recently discovered formulas shown by Eqs. (27), (38), and (45) in Ref. [12]. These equations convert the evaluation of periodic orbit actions into the calculation of action differences between certain auxiliary homoclinic orbits constructed from the symbolic codes of the periodic orbit. Therefore, upon the determination of homoclinic orbit actions, the determination of periodic orbit actions becomes a simple manipulation of symbolic strings and subtractions within the homoclinic action set, a trivial task that poses no serious difficulties. Therefore, just like the homoclinic orbit actions, the exponentially increasing set of periodic orbit actions is expressible with the same reduced set of cell areas as well. Further extension of the current method concerns the stability exponents of unstable periodic orbits, which is a topic under current investigation.

## Appendix A: Systematic assignments of symbolic codes

Although the symbolic codes of some simple homoclinic orbits, such as the primary ones, can be easily determined by following the numerical orbits, such tasks become prohibitive for the exponentially proliferating ensemble of more complicated, non-primary orbits. In addition, a computational method does not reveal the patterns and structural relations buried in substrings of the symbolic codes. In fact, as shown by [55], symbolic codes provide a natural ordering of homoclinic points along the



fundamental segments, which is otherwise unattainable from numerical methods. Although this problem is essentially solved by [55] for the Hénon maps in the complete horseshoe region, their approach starts from the anti-intergable limit [56, 57], and identifies each homoclinic orbit near the limit as continuations from the anti-integrable limit. Although exact and efficient, it does not make use of the accumulation relations (Sec. III B) which are the theoretical foundations of the present paper. This appendix introduces a different approach. Taking advantage of the hierarchical structure of the homoclinic orbits (see Sec. III), a recursive scheme is introduced that systematically determines the symbolic codes of the families of winding- $(n+1)$  homoclinic orbits based on the symbolic code of the winding- $n$  orbit on which they accumulate. It results in an ordering of homoclinic points on the fundamental segment  $S_{-1}$  in terms of their symbolic codes, which is equivalent to Lemma 7 of [55] upon switching the alphabets “0”  $\rightarrow$  “+” and “1”  $\rightarrow$  “-”. This provides a foundation for the exact relations and approximations of Sec. IV.

Every homoclinic orbit has one and only one representative point on  $S_{-1}$  and labeling the entire set of orbits can be reduced to labeling the homoclinic points on  $S_{-1}$ . Starting from  $T_{-1,-1}$ , in which  $S_{-1}$  is not intersected by any unstable fundamental segment, the only homoclinic points are the primaries  $h_{-1} \Rightarrow \bar{0}.11\bar{0}$  and  $g_{-2} \Rightarrow \bar{0}.01\bar{0}$ , both of which are winding-1. Proceeding to the intersections of  $S_{-1}$  with  $T_{-1,0}$ , there are two winding-2 points,  $a^{(0)}$  and  $b^{(0)}$ , as shown by Fig. 12, which are the leading

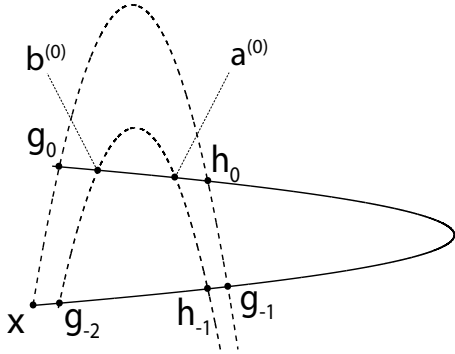


FIG. 12. Homoclinic points in  $T_{-1,0}$ . The symbolic codes are:  $h_{-1} \Rightarrow \bar{0}.11\bar{0}$ ,  $g_{-2} \Rightarrow \bar{0}.01\bar{0}$ ,  $a^{(0)} \Rightarrow \bar{0}1.11\bar{0}$ , and  $b^{(0)} \Rightarrow \bar{0}1.01\bar{0}$ . The hierarchical relations are:  $a^{(0)}, b^{(0)} \xrightarrow{\frac{1}{S}} g_{-2}$ . Notice that the hierarchical relations are indicative for the assignments of symbolic codes: the codes of  $a^{(0)}$  and  $b^{(0)}$  can be obtained by adding the substrings “11” and “10”, respectively, to the left end of the core of  $g_{-2}$ , while maintaining the position of the decimal point relative to the right end of the core.

terms of the two winding-2 families  $[a^{(n)}]$  and  $[b^{(n)}]$  from the future  $T_{-1,n}$  that accumulate on  $g_{-2}$ . Their symbolic codes are  $a^{(0)} \Rightarrow \bar{0}1.11\bar{0}$  and  $b^{(0)} \Rightarrow \bar{0}1.01\bar{0}$ , which emerges quickly by following their excursions. The hierarchical relationship at this stage can be denoted alter-

natively as

$$\begin{aligned} (a^{(0)} \Rightarrow \bar{0}1.11\bar{0}) &\xrightarrow{\frac{1}{S}} (g_{-2} \Rightarrow \bar{0}.01\bar{0}) \\ (b^{(0)} \Rightarrow \bar{0}1.01\bar{0}) &\xrightarrow{\frac{1}{S}} (g_{-2} \Rightarrow \bar{0}.01\bar{0}) \end{aligned} \quad (\text{A1})$$

where the notations “ $\frac{1}{S}$ ” are defined in Eq. (19). Notice that the hierarchical relations imply the symbolic code assignments: the codes of  $a^{(0)}$  and  $b^{(0)}$  can be obtained by adding the substrings “11” and “10”, respectively, to the left end of the core of  $g_{-2}$ , while maintaining the position of the decimal point relative to the right end of the core. Also, the transit times of  $a^{(0)}$  and  $b^{(0)}$  are both unity, and their core lengths are both 3. It turns out in general that

$$\text{core length} = \text{transit time} + 2, \quad (\text{A2})$$

which holds true for all non-primary homoclinic points. Another important observation is,  $a^{(0)}$  and  $b^{(0)}$  with core lengths 3, emerged from  $S_{-1} \cap U_0$  in trellis  $T_{-1,0}$ . This leads to the simple fact that any non-primary homoclinic point that emerges from  $S_{-1} \cap U_n$  in  $T_{-1,n}$  must have core length  $n+3$ .

There are four new intersections generated by  $T_{-1,1}$ , i.e.,  $S_{-1} \cap U_1$ . Figure 13 shows the four new winding-2 points labeled  $a^{(1)}$ ,  $b^{(1)}$ ,  $c^{(1)}$ , and  $d^{(1)}$ . An important distinction between them is:  $a^{(1)}$  and  $b^{(1)}$  are the

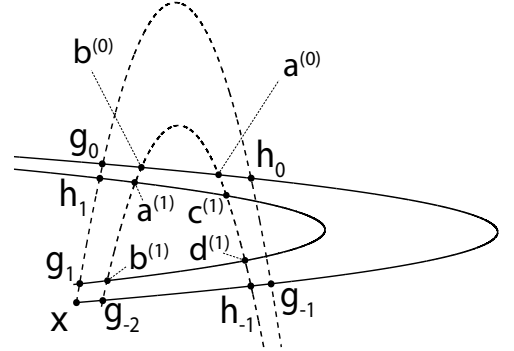


FIG. 13. Homoclinic points in  $T_{-1,1}$ . The symbolic codes are:  $a^{(1)} \Rightarrow \bar{0}11.01\bar{0}$ ,  $b^{(1)} \Rightarrow \bar{0}10.01\bar{0}$ ,  $c^{(1)} \Rightarrow \bar{0}11.11\bar{0}$ , and  $d^{(1)} \Rightarrow \bar{0}10.11\bar{0}$ . The hierarchical relations are:  $a^{(1)}, b^{(1)} \xrightarrow{\frac{2}{S}} g_{-2}$  and  $c^{(1)}, d^{(1)} \xrightarrow{\frac{1}{S}} h_{-1}$ .

second realizations of their respective families  $[a^{(n)}]$  and  $[b^{(n)}]$  ( $n \geq 0$ ) that accumulate on  $g_{-2}$ , whereas  $c^{(1)}$  and  $d^{(1)}$  are the first terms of their respective families,  $[c^{(n)}]$  and  $[d^{(n)}]$  ( $n \geq 1$ ), that accumulate on  $h_{-1}$ . Therefore, following the pattern of Eq. (A1), the symbolic codes of  $c^{(1)}$  and  $d^{(1)}$  should be obtained by adding the substring “11” and “10”, respectively, to the left end of the core of  $h_{-1}$  (which is “11”), while keeping the position of the decimal point relative to the right end of the core. This leads to



the assignments  $c^{(1)} \Rightarrow \bar{0}11.11\bar{0}$  and  $d^{(1)} \Rightarrow \bar{0}10.11\bar{0}$  according to the hierarchical relations

$$\begin{aligned} (c^{(1)} \Rightarrow \bar{0}11.11\bar{0}) &\xrightarrow[S]{1} (h_{-1} \Rightarrow \bar{0}.11\bar{0}) \\ (d^{(1)} \Rightarrow \bar{0}10.11\bar{0}) &\xrightarrow[S]{1} (h_{-1} \Rightarrow \bar{0}.11\bar{0}). \end{aligned} \quad (\text{A3})$$

As for the symbolic codes of  $a^{(1)}$  and  $b^{(1)}$ , since they are the second terms in their respective accumulating families, the substrings “110” and “100”, instead of “11” and “10”, should be added to the left end of the core of  $g_{-2}$ , respectively, while keeping the position of the decimal point relative to the right end of the core unchanged:

$$\begin{aligned} (a^{(1)} \Rightarrow \bar{0}11.01\bar{0}) &\xrightarrow[S]{2} (g_{-2} \Rightarrow \bar{0}.01\bar{0}) \\ (b^{(1)} \Rightarrow \bar{0}10.01\bar{0}) &\xrightarrow[S]{2} (g_{-2} \Rightarrow \bar{0}.01\bar{0}). \end{aligned} \quad (\text{A4})$$

Calculating the orbits numerically, one readily verifies that Eqs. (A3) and (A4) indeed give the correct desired symbolic codes for the orbits.

Generalization of the above relations gives the general rule for the assignment of symbolic codes. Given an arbitrary winding- $m$  homoclinic point  $y$ , and two winding- $(m+1)$  homoclinic points  $z$  and  $w$  from the two winding- $(m+1)$  families accumulating on  $y$ , such that  $z \xrightarrow[S]{k} y$  and  $w \xrightarrow[S]{k} y$  ( $k \geq 1$ ) and  $S[y, w] \subset S[y, z]$ , then the symbolic codes of  $z$  and  $w$  can be obtained by adding the substrings “110 $^{k-1}$ ” and “100 $^{k-1}$ ”, respectively, to the left end of the core of  $y$ , keeping the position of the decimal point relative to the right end of the core. The notation “0 $^{k-1}$ ” denotes a string composed of  $(k-1)$  consecutive “0”s. Or equivalently, let the symbolic code of the orbit  $\{y\}$  be  $\{y\} \Rightarrow \bar{0}\tilde{\gamma}\bar{0}$ , where the string  $\tilde{\gamma}$  denotes the core, then the symbolic codes of orbits  $\{z\}$  and  $\{w\}$  are determined as

$$\begin{aligned} \{z\} &\Rightarrow \bar{0}110^{k-1}\tilde{\gamma}\bar{0} \\ \{w\} &\Rightarrow \bar{0}100^{k-1}\tilde{\gamma}\bar{0} \end{aligned} \quad (\text{A5})$$

and the position of the decimal points in the symbolic codes of  $z$  and  $w$  are identical to that of  $y$ , when counted from the right ends of their cores.

Concrete examples of the preceding assignment rules are labeled in Fig. 3. Choose the winding-2 point  $a^{(0)} \Rightarrow \bar{0}1.11\bar{0}$  as the base, and notice the accumulating points  $e^{(k)}, f^{(k)} \xrightarrow[S]{k} a^{(0)}$ , where the  $k = 1, 2$  cases are explicitly shown in the figure. According to the preceding assignment rules, the symbolic codes of  $e^{(k)}$  and  $f^{(k)}$  are constructed as  $f^{(k)} \Rightarrow \bar{0}110^{k-1}.11\bar{0}$  and  $e^{(k)} \Rightarrow \bar{0}100^{k-1}.11\bar{0}$ , which was verified numerically.

The proof of Eq. (A5) involves mapping the base point  $y$  simultaneously with  $z$  and  $w$  forward and inversely, to study the deformation of  $S[y, z/w]$  under forward iterations, and the deformation of  $U[y, z/w]$  under inverse

iterations. Notice that the stable segments  $S[y, z/w]$  belong to either  $S[g_{-2}, b^{(0)}]$  or  $S[h_{-1}, a^{(0)}]$ , which will become even shorter under forward iterations. Therefore, forward iterations of  $y$  and  $z/w$  are guaranteed to locate on the same side of  $S_{-1}$ , thus in the same generating partition ( $V_0$  or  $V_1$ ). For the inverse mappings, the unstable segments  $U[y, z/w]$  are constrained to deform in a specific way such that the images of  $y$  and  $z/w$  must locate in the same partition along the code segment “0 $^{k-1}\tilde{\gamma}$ ” first. After that, the backward images of  $z$  immediately visit  $V_1$  twice, then stay in  $V_0$  as they approach  $x$ ; on the contrary, the backward images of  $w$  visit  $V_0$  and  $V_1$  consecutively, and then stay in  $V_0$  as they approach  $x$ . The slight difference in their behaviors give rise to the “ $\bar{0}11$ ” and “ $\bar{0}10$ ” in their respective symbolic codes in Eq. (A5). The detailed derivation is quite lengthy and skipped here for brevity.

With Eq. (A5), the complete set of symbolic codes is generated based on just the symbolic codes of the two primary orbits. For a finite trellis  $T_{-1, N}$  (presumably with large  $N$ ), the maximum transition time of homoclinic orbits is  $N+1$ , i.e., those arise from  $S_{-1} \cap U_N$ . According to Eq. (A2), the corresponding maximum core length is  $N+3$ . Therefore, starting from  $\{h_{-1}\} \Rightarrow \bar{0}11\bar{0}$  and  $\{g_{-2}\} \Rightarrow \bar{0}1\bar{0}$ , by intersecting  $S_{-1}$  with successive  $U_i$  where  $0 \leq i \leq N$  and recursive use of Eq. (A5) up to core length  $N+3$ , the symbolic codes of all homoclinic orbits present in  $T_{-1, N}$  are generated according to the relative positions of their representative points on  $S_{-1}$ . This process is equivalent to the  $>_s$  ordering in Lemma 7 of [55].

A similar prescription could have been generated for the accumulating homoclinic families along the unstable manifold under inverse mappings. Given any winding- $n$  homoclinic point  $y'$ , and two winding- $(n+1)$  homoclinic points  $z'$  and  $w'$  such that  $z' \xrightarrow[U]{k} y'$ ,  $w' \xrightarrow[U]{k} y'$  ( $k \geq 1$ ) and  $U[y', w'] \subset U[y', z']$ , the symbolic codes of  $z'$  and  $w'$  can be constructed by adding the substrings “0 $^{k-1}11$ ” and “0 $^{k-1}01$ ”, respectively, to the right end of the core of the symbolic code of  $y'$ , while keeping the position of the decimal point relative to the left end of the core unchanged. Or equivalently, if we let the symbolic code of the orbit be  $\{y'\} \Rightarrow \bar{0}\tilde{\gamma}'\bar{0}$  where  $\tilde{\gamma}'$  denotes the core, then the symbolic codes of orbits  $\{z'\}$  and  $\{w'\}$  are constructed as

$$\begin{aligned} \{z'\} &\Rightarrow \bar{0}\tilde{\gamma}'0^{k-1}11\bar{0} \\ \{w'\} &\Rightarrow \bar{0}\tilde{\gamma}'0^{k-1}01\bar{0} \end{aligned} \quad (\text{A6})$$

which is in complete analogy to Eq. (A5), and equivalent to the  $>_u$  ordering in Lemma 7 of [55]. For example, in Fig. 4 we have  $g_0 \Rightarrow \bar{0}1.\bar{0}$ , and  $v^{(-k)}, w^{(-k)} \xrightarrow[U]{k} g_0$ , where the  $k = 1, 2$  cases are explicitly shown in the figure. Then according to the preceding rules, the symbolic codes of  $v^{(-k)}$  and  $w^{(-k)}$  are constructed from the symbolic code of  $g_0$  as  $v^{(-k)} \Rightarrow \bar{0}1.0^{k-1}11\bar{0}$  and  $w^{(-k)} \Rightarrow \bar{0}1.0^{k-1}01\bar{0}$ , respectively.



## Appendix B: Asymptotic accumulation exponent

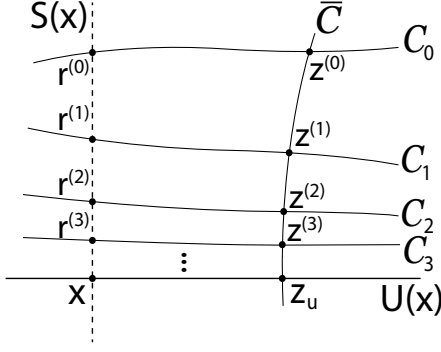


FIG. 14. (Schematic) Iterates of a curve intersecting the stable manifold approach the unstable manifold. Future iterations of the curve  $C_0$  creates a family of curves  $[C_n]$ , which intersect  $\bar{C}$  at a family of points  $[z^{(n)}]$ .  $[z^{(n)}]$  accumulates on  $z_u$  under the exponent  $\mu_x$ , as given by Eq. (B1).

The foundation of Sec. IIIB is established by Lemma 2 in Appendix. B. 3 of [38], and a brief overview of their results is given here. The setting of the lemma is demonstrated schematically by Fig. 14. Let  $z_u$  be an arbitrary point on  $U(x)$ , and  $\bar{C}$  an arbitrary differentiable curve passing transversely through  $U(x)$  at  $z_u$ . Consider another arbitrary differentiable curve,  $C_0$ , which passes through  $S(x)$  transversely at  $r^{(0)}$ , and intersects  $\bar{C}$  at  $z^{(0)}$ . Then, its future iterations  $C_n = M^n(C_0)$  ( $n \geq 1$ ) pass through  $S(x)$  transversely at  $r^{(n)}$ , and intersect  $\bar{C}$  at  $z^{(n)}$ , which form a family of points  $[z^{(n)}]$  that accumulate asymptotically on the base point  $z_u$ :

$$\begin{aligned} \lim_{n \rightarrow \infty} z^{(n)} &= z_u \\ \lim_{n \rightarrow \infty} \|z^{(n)} - z_u\| e^{n\mu_x} &= C(z_u, z^{(0)}) \end{aligned} \quad (\text{B1})$$

where  $\|\cdot\|$  is the standard Euclidean vector norm,  $\mu_x$  is the stability exponent of  $x$ , and  $C(z_u, z^{(0)})$  is a positive constant depending on the base point  $z_u$  and the leading term  $z^{(0)}$  in the asymptotic family. Notice that Eq. (B1) is just a re-expression of Eqs. (B5) and (B6) of [38]. What is surprising here is that even though the manifolds explore the vast majority of phase space with clearly non-uniform expansion rates, the asymptotic exponent in the above equation is still that of the hyperbolic fixed point.

## Appendix C: Area correspondence relations

Given any homoclinic point  $y \in (S_{-1} \cap U_m)$ , there is an explicit relation that links  $\mathcal{A}_{SUSU}^\circ[y, P_S(y), P_S P_U(y), P_U(y)]$  with specific linear combinations of cell areas from the type-I and type-II partition trees of  $T_{-1,m}$ . The transition time of  $y$  is  $m+1$ , so its core length is  $m+3$ . Let  $\tilde{\gamma} = s_1 s_2 \cdots s_{m+2} s_{m+3}$  ( $s_i \in \{0,1\}$ ,  $s_1 = s_{m+3} = 1$ ) be the core of the symbolic code of  $y$ , then the linear

combination of cell areas depends solely on  $\tilde{\gamma}$ . The correspondence relation is established in the following step.

- 1) Define  $\Phi_{B \mapsto A}$  to be a mapping from the cells of the type-II partition trees to the cells of the type-I partition trees, such that for any finite Greek alphabet string  $\tilde{\omega}$  composed of  $\alpha$ ,  $\gamma$ , and  $\beta$  ( $\tilde{\omega}$  could also be an empty string) we have

$$\begin{cases} \Phi_{B \mapsto A}(B_{\tilde{\omega}}) = A_{\tilde{\omega}} \\ \Phi_{B \mapsto A}(A_{\tilde{\omega}}) = \emptyset \\ \Phi_{B \mapsto A}(\emptyset) = \emptyset \end{cases} \quad (\text{C1})$$

where  $\emptyset$  denotes a null cell that gives zero contribution to the action calculations.

- 2) Define  $\Phi_{\beta \mapsto \alpha}$  to be a mapping between the cells of the partition trees, such that for any finite Greek alphabet string  $\tilde{\omega}$  composed of  $\alpha$  and  $\gamma$  (but not  $\beta$ , note also that  $\tilde{\omega}$  could be an empty string), we have

$$\begin{cases} \Phi_{\beta \mapsto \alpha}(A_{\tilde{\omega}\beta}) = A_{\tilde{\omega}\alpha} \\ \Phi_{\beta \mapsto \alpha}(B_{\tilde{\omega}\beta}) = B_{\tilde{\omega}\alpha} \\ \Phi_{\beta \mapsto \alpha}(A_{\tilde{\omega}\alpha}) = \Phi_{\beta \mapsto \alpha}(B_{\tilde{\omega}\alpha}) = \emptyset \\ \Phi_{\beta \mapsto \alpha}(A) = \Phi_{\beta \mapsto \alpha}(B) = \emptyset \\ \Phi_{\beta \mapsto \alpha}(\emptyset) = \emptyset \end{cases} \quad (\text{C2})$$

- 3) Define  $\Gamma$  to be a mapping from the core  $\tilde{\gamma} = s_1 s_2 \cdots s_{m+2} s_{m+3}$  ( $s_1 = s_{m+3} = 1$ ) of the symbolic code of any non-primary homoclinic point  $y \in (S_{-1} \cap U_m)$  to the cells of the partition trees, such that depending on the detailed forms of  $\tilde{\gamma}$ , the mapping  $\Gamma$  takes the forms:

$$\Gamma(\tilde{\gamma}) = \begin{cases} \Gamma(101) = A \\ \Gamma(111) = B \\ \Gamma\left(\begin{smallmatrix} 10 & \cdots & 0 & \cdots & 1 & \cdots & 01 \\ \downarrow & & \downarrow & & \downarrow & & \downarrow \\ \alpha & \cdots & \alpha & \cdots & \gamma & \cdots & A \end{smallmatrix}\right) = A_{\alpha \cdots \gamma \cdots \alpha \cdots \alpha} \\ \Gamma\left(\begin{smallmatrix} 10 & \cdots & 0 & \cdots & 1 & \cdots & 11 \\ \downarrow & & \downarrow & & \downarrow & & \downarrow \\ \alpha & \cdots & \alpha & \cdots & \gamma & \cdots & B \end{smallmatrix}\right) = B_{\alpha \cdots \gamma \cdots \alpha \cdots \alpha} \\ \Gamma\left(\begin{smallmatrix} 11 & \cdots & 0 & \cdots & 1 & \cdots & 01 \\ \downarrow & & \downarrow & & \downarrow & & \downarrow \\ \beta & \cdots & \alpha & \cdots & \gamma & \cdots & A \end{smallmatrix}\right) = A_{\beta \cdots \alpha \cdots \gamma \cdots \beta} \\ \Gamma\left(\begin{smallmatrix} 11 & \cdots & 0 & \cdots & 1 & \cdots & 11 \\ \downarrow & & \downarrow & & \downarrow & & \downarrow \\ \beta & \cdots & \alpha & \cdots & \gamma & \cdots & B \end{smallmatrix}\right) = B_{\beta \cdots \alpha \cdots \gamma \cdots \beta} \end{cases} \quad (\text{C3})$$



in which the  $\tilde{\gamma} = 101$  and  $\tilde{\gamma} = 111$  cases yield cells  $A$  and  $B$ , respectively; and all the rest of cases with core lengths  $\geq 4$  (or equivalently  $m \geq 1$ ) are categorized into four cases,  $\{s_2 = 0, s_{m+2} = 0\}$ ,  $\{s_2 = 0, s_{m+2} = 1\}$ ,  $\{s_2 = 1, s_{m+2} = 0\}$ , and  $\{s_2 = 1, s_{m+2} = 1\}$ , which correspond to the third, fourth, fifth, and sixth line of Eq. (C3), respectively. Notice in those four cases, the letters  $A$  and  $B$  of the cell names are given by the last two digits  $s_{m+2}s_{m+3}$  of  $\tilde{\gamma}$  with grammar “ $01 \mapsto A$ ” and “ $11 \mapsto B$ ”. The Greek alphabet string of the cell names are given by the first  $m+1$  digits of  $\tilde{\gamma}$  in an reversed order:  $s_1s_2$  gives the last alphabet in the Greek string, with grammar “ $10 \mapsto \alpha$ ” and “ $11 \mapsto \beta$ ”; and  $s_{m+1}s_m \cdots s_4s_3$  (reversed string of  $s_3s_4 \cdots s_ms_{m+1}$ ) gives the first  $m-1$  alphabets in the Greek string, with grammar “ $0 \mapsto \alpha$ ” and “ $1 \mapsto \gamma$ ”.

- 4) Finally, the  $\mathcal{A}_{SUSU[y, P_S(y), P_S P_U(y), P_U(y)]}^\circ$  area can be calculated as

$$\begin{aligned} \mathcal{A}_{SUSU[y, P_S(y), P_S P_U(y), P_U(y)]}^\circ &= (-1)^{n_\gamma(\Gamma(\tilde{\gamma}))} \cdot \left[ \Gamma(\tilde{\gamma}) \right. \\ &\quad \left. + \Phi_{\beta \mapsto \alpha}(\Gamma(\tilde{\gamma})) + \Phi_{B \mapsto A}(\Gamma(\tilde{\gamma})) + \Phi_{B \mapsto A}(\Phi_{\beta \mapsto \alpha}(\Gamma(\tilde{\gamma}))) \right] \end{aligned} \quad (C4)$$

where  $n_\gamma(\Gamma(\tilde{\gamma}))$  is a function that returns the total number of  $\gamma$  in the Greek alphabet string of the cell  $\Gamma(\tilde{\gamma})$ . For example,  $n_\gamma(A_{\alpha\beta}) = 0$  and  $n_\gamma(B_{\gamma\beta}) = 1$ . Again, we emphasize that Eq. (C4) only applies to non-primary homoclinic points  $y$  located on  $S_{-1}$ .

Eq. (C4) gives a systematic way of identifying the  $\mathcal{A}_{SUSU[y, P_S(y), P_S P_U(y), P_U(y)]}^\circ$  term in the homoclinic action decomposition [Eq. (36)] in terms of a linear combination of cell areas from the type-I and type-II partition trees. In practice, some of the terms in Eq. (C4) will vanish due to the presence of null areas ( $\emptyset$ ) in Eqs. (C1) and (C2). Depending on  $y$ , Eq. (C4) may take four possible forms, as listed below:

- 1) A single type-I cell area:  $A$  (for  $y=b^{(0)}$  only) or  $A_{\tilde{\omega}\alpha}$ , where  $\tilde{\omega}$  denotes some Greek alphabet string composed by  $\alpha$  and  $\gamma$ . Examples are

- i) In Fig. 12, let  $y = b^{(0)} \in (S_{-1} \cap U_0)$ , then

$$\begin{aligned} \mathcal{A}_{SUSU[y, P_S(y), P_S P_U(y), P_U(y)]}^\circ &= \mathcal{A}_{SUSU[b^{(0)}, g_{-2}, x, g_0]}^\circ = A, \end{aligned}$$

which a type-I cell of  $T_{-1,0}$ .

- ii) In Fig. 5, let  $y = b^{(1)} \in (S_{-1} \cap U_1)$ , then

$$\begin{aligned} \mathcal{A}_{SUSU[y, P_S(y), P_S P_U(y), P_U(y)]}^\circ &= \mathcal{A}_{SUSU[b^{(1)}, g_{-2}, x, g_1]}^\circ = A_\alpha, \end{aligned}$$

which a type-I cell of  $T_{-1,1}$ .

- iii) In Fig. 8, let  $y = r^{(1)} \in (S_{-1} \cap U_2)$ , then

$$\begin{aligned} \mathcal{A}_{SUSU[y, P_S(y), P_S P_U(y), P_U(y)]}^\circ &= \mathcal{A}_{SUSU[r^{(1)}, b^{(0)}, g_0, v]}^\circ = -A_{\gamma\alpha}, \end{aligned}$$

which is a type-I cell area of  $T_{-1,2}$ .

- 2) Two type-I areas:  $A_{\tilde{\omega}\beta} + A_{\tilde{\omega}\alpha}$ . Examples are

- i) In Fig. 5, let  $y = a^{(1)} \in (S_{-1} \cap U_1)$ , then

$$\begin{aligned} \mathcal{A}_{SUSU[y, P_S(y), P_S P_U(y), P_U(y)]}^\circ &= \mathcal{A}_{SUSU[a^{(1)}, g_{-2}, x, h_1]}^\circ = A_\beta + A_\alpha, \end{aligned}$$

which is the sum of two type-I areas of  $T_{-1,1}$ .

- ii) In Fig. 8, let  $y = s^{(1)} \in (S_{-1} \cap U_2)$ , then

$$\begin{aligned} \mathcal{A}_{SUSU[y, P_S(y), P_S P_U(y), P_U(y)]}^\circ &= \mathcal{A}_{SUSU[s^{(1)}, b^{(0)}, g_0, w]}^\circ = -(A_{\gamma\beta} + A_{\gamma\alpha}), \end{aligned}$$

which is the sum of two type-I areas of  $T_{-1,2}$ .

- 3) A type-I area and a type-II area:  $A+B$  (for  $y = a^{(0)}$  only) or  $A_{\tilde{\omega}\alpha} + B_{\tilde{\omega}\alpha}$ . Examples are

- i) In Fig. 12, let  $y = a^{(0)} \in (S_{-1} \cap U_0)$ . Recall that only for the special case of  $y = a^{(0)}$ , we alter Eq. (36) into Eq. (40), whose area term gives

$$\mathcal{A}_{SUSU[a^{(0)}, h_{-1}, x, g_0]}^\circ = A + B$$

which is the sum of a type-I and a type-II area of  $T_{-1,0}$ .

- ii) In Fig. 5, let  $y = d^{(1)} \in (S_{-1} \cap U_1)$ , then

$$\begin{aligned} \mathcal{A}_{SUSU[y, P_S(y), P_S P_U(y), P_U(y)]}^\circ &= \mathcal{A}_{SUSU[d^{(1)}, h_{-1}, x, g_1]}^\circ = A_\alpha + B_\alpha, \end{aligned}$$

which is the sum of a type-I and a type-II area.

- iii) In Fig. 8, let  $y = e^{(1)} \in (S_{-1} \cap U_2)$ , then

$$\begin{aligned} \mathcal{A}_{SUSU[y, P_S(y), P_S P_U(y), P_U(y)]}^\circ &= \mathcal{A}_{SUSU[e^{(1)}, a^{(0)}, g_0, v]}^\circ = -(A_{\gamma\alpha} + B_{\gamma\alpha}), \end{aligned}$$

which is the sum of a type-I and a type-II area of  $T_{-1,2}$ .

- 4) Two type-I areas plus two type-II areas:  $A_{\tilde{\omega}\alpha} + A_{\tilde{\omega}\beta} + B_{\tilde{\omega}\alpha} + B_{\tilde{\omega}\beta}$ . Examples are

- i) In Fig. 5, let  $y = c^{(1)} \in (S_{-1} \cap U_1)$ , then

$$\begin{aligned} \mathcal{A}_{SUSU[y, P_S(y), P_S P_U(y), P_U(y)]}^\circ &= \mathcal{A}_{SUSU[c^{(1)}, h_{-1}, x, h_1]}^\circ \\ &= A_\alpha + A_\beta + B_\alpha + B_\beta, \end{aligned}$$

which is the sum of two type-I and two type-II areas of  $T_{-1,1}$ .



ii) In Fig. 8, let  $y = f^{(1)} \in (S_{-1} \cap U_2)$ , then

$$\begin{aligned} \mathcal{A}_{SUSU}^{\circ}[y, P_S(y), P_S P_U(y), P_U(y)] \\ = \mathcal{A}_{SUSU}^{\circ}[f^{(1)}, a^{(0)}, g_0, w] \\ = -(A_{\gamma\alpha} + A_{\gamma\beta} + B_{\gamma\alpha} + B_{\gamma\beta}), \end{aligned}$$

which is the sum of two type-I and two type-II

areas of  $T_{-1,2}$ .

## ACKNOWLEDGMENTS

JL gratefully acknowledges many inspiring discussions with Akira Shudo during several productive visits to Tokyo Metropolitan University.

- 
- [1] P. Cvitanović, R. Artuso, R. Mainieri, G. Tanner, and G. Vattay, *Chaos: Classical and Quantum* (Niels Bohr Inst., Copenhagen, 2016).
  - [2] P. So, *Scholarpedia* **2**, 1353 (2007).
  - [3] M. C. Gutzwiller, *J. Math. Phys.* **12**, 343 (1971), and references therein.
  - [4] M. L. Du and J. B. Delos, *Phys. Rev. A* **38**, 1896 (1988).
  - [5] M. L. Du and J. B. Delos, *Phys. Rev. A* **38**, 1913 (1988).
  - [6] S. Tomsovic and E. J. Heller, *Phys. Rev. E* **47**, 282 (1993).
  - [7] G. D. Birkhoff, *Acta Math.* **50**, 359 (1927).
  - [8] J. Moser, *Commun. Pure Appl. Math.* **9**, 673 (1956).
  - [9] G. L. da Silva Ritter, A. M. Ozorio de Almeida, and R. Douady, *Physica D* **29**, 181 (1987).
  - [10] A. M. Ozorio de Almeida, *Nonlinearity* **2**, 519 (1989).
  - [11] J. Li and S. Tomsovic, *Phys. Rev. E* **95**, 062224 (2017), arXiv:1703.07045 [nlin.CD].
  - [12] J. Li and S. Tomsovic, *Phys. Rev. E* **97**, 022216 (2018), arXiv:1712.05568 [nlin.CD].
  - [13] R. S. MacKay, J. D. Meiss, and I. C. Percival, *Physica D* **13**, 55 (1984).
  - [14] J. D. Meiss, *Rev. Mod. Phys.* **64**, 795 (1992).
  - [15] E. J. Doedel and M. J. Friedman, *J. Comput. Appl. Math.* **26**, 155 (1989).
  - [16] W. J. Beyn, *IMA J. Numer. Anal.* **9**, 379 (1990).
  - [17] G. Moore, *IMA J. Numer. Anal.* **15**, 245 (1995).
  - [18] J. Li and S. Tomsovic, *J. Phys. A: Math. Theor.* **50**, 135101 (2017), arXiv:1507.06455 [nlin.CD].
  - [19] A. A. Brudno, *Russ. Math. Surv.* **33**, 197 (1978).
  - [20] V. M. Alekseev and M. V. Yakobson, *Phys. Rep.* **75**, 287 (1981).
  - [21] A. N. Kolmogorov, *Doklady of Russian Academy of Sciences* **119**, 861 (1958).
  - [22] A. N. Kolmogorov, *Doklady of Russian Academy of Sciences* **124**, 754 (1959).
  - [23] Y. G. Sinai, *Doklady of Russian Academy of Sciences* **124**, 768 (1959).
  - [24] Y. B. Pesin, *Russ. Math. Surv.* **32**, 55 (1977).
  - [25] P. Gaspard and G. Nicolis, *Phys. Rev. Lett.* **65**, 1693 (1990).
  - [26] A. Connes, H. Narnhofer, and W. Thirring, *Commun. Math. Phys.* **112**, 691 (1987).
  - [27] R. Alicki and M. Fannes, *Math. Phys.* **32**, 75 (1994).
  - [28] G. Lindblad, in *Quantum Probability and Applications*, edited by L. Accardi and W. von Waldenfels (Springer, Berlin, 1988) pp. 183–191, vol. III.
  - [29] P. Cvitanović, *Chaos* **2**, 1 (1992).
  - [30] P. Cvitanović, *Phys. Rev. Lett.* **61**, 2729 (1988).
  - [31] P. Cvitanović and B. Eckhardt, *Phys. Rev. Lett.* **63**, 823 (1989).
  - [32] E. B. Bogomolny, *Chaos* **2**, 5 (1992).
  - [33] L. Kaplan, *Phys. Rev. Lett.* **81**, 3371 (1998).
  - [34] H. Poincaré, *Les méthodes nouvelles de la mécanique céleste*, Vol. 3 (Gauthier-Villars et fils, Paris, 1899).
  - [35] R. W. Easton, *Trans. Am. Math. Soc.* **294**, 719 (1986).
  - [36] V. Rom-Kedar, *Physica D* **43**, 229 (1990).
  - [37] S. Wiggins, *Chaotic Transport in Dynamical Systems* (Springer, New York, 1992).
  - [38] K. A. Mitchell, J. P. Handley, B. Tighe, J. B. Delos, and S. K. Knudson, *Chaos* **13**, 880 (2003).
  - [39] K. A. Mitchell, J. P. Handley, J. B. Delos, and S. K. Knudson, *Chaos* **13**, 892 (2003).
  - [40] K. A. Mitchell and J. B. Delos, *Physica D* **221**, 170 (2006).
  - [41] J. Novick, M. L. Keeler, J. Giefer, and J. B. Delos, *Phys. Rev. E* **85**, 016205 (2012).
  - [42] J. Novick and J. B. Delos, *Phys. Rev. E* **85**, 016206 (2012).
  - [43] J. Hadamard, *J. Math. Pures Appl. series 5* **4**, 27 (1898).
  - [44] G. D. Birkhoff, *A.M.S. Coll. Publications, vol. 9* (American Mathematical Society, Providence, 1927).
  - [45] G. D. Birkhoff, *Mem. Pont. Acad. Sci. Novi Lyncae* **1**, 85 (1935).
  - [46] M. Morse and G. A. Hedlund, *Amer. J. Math.* **60**, 815 (1938).
  - [47] R. Bowen, *Lect. Notes in Math. Vol. 470*. (Springer-Verlag, Berlin, 1975).
  - [48] P. Gaspard, *Chaos, Scattering and Statistical Mechanics* (Cambridge University Press, Cambridge, UK, 1998).
  - [49] S. Smale, *Differential and Combinatorial Topology*, edited by S. S. Cairns (Princeton University Press, Princeton, 1963).
  - [50] S. Smale, *The Mathematics of Time: Essays on Dynamical Systems, Economic Processes and Related Topics* (Springer-Verlag, New York, Heidelberg, Berlin, 1980).
  - [51] P. Cvitanović, G. Gunaratne, and I. Procaccia, *Phys. Rev. A* **38**, 1503 (1988).
  - [52] P. Cvitanović, *Physica D* **51**, 138 (1991).
  - [53] M. Hénon, *Comm. Math. Phys.* **50**, 69 (1976).
  - [54] R. Hagiwara and A. Shudo, *J. Phys. A: Math. Gen.* **37**, 10521–10543 (2004).
  - [55] D. Sterling, H. R. Dullin, and J. D. Meiss, *Physica D* **134**, 153 (1999).
  - [56] S. Aubry and G. Abramovici, *Physica D* **43**, 199 (1990).
  - [57] S. Aubry, *Physica D* **86**, 284 (1995).
  - [58] K. Hockett and P. Holmes, *Ergod. Th. & Dynam. Sys.* **6**, 205 (1986).
  - [59] D. Bevilaqua and M. Basílio de Matos, *Physica D* **145**, 13 (2000).